

A phase-field lattice Boltzmann model for simulating multiphase flows in porous media: Application and comparison to experiments of CO₂ sequestration at pore scale

Abbas Fakhari^a, Yaofa Li^{b,c}, Diogo Bolster^{a,c,*}, Kenneth T. Christensen^{a,b,c}

^a Department of Civil and Environmental Engineering and Earth Sciences, University of Notre Dame, Notre Dame, IN 46556, USA

^b Department of Mechanical and Aerospace Engineering, University of Notre Dame, Notre Dame, IN 46556, USA

^c International Institute for Carbon-Neutral Energy Research (I2CNER), Kyushu University, Japan

ARTICLE INFO

Article history:

Received 4 October 2017

Revised 28 December 2017

Accepted 5 February 2018

Available online 10 February 2018

Keywords:

CO₂ Sequestration

Lattice Boltzmann method

Porous micromodel

Capillary fingering

Viscous fingering

Pore-scale modeling

ABSTRACT

We implement a phase-field based lattice-Boltzmann (LB) method for numerical simulation of multiphase flows in heterogeneous porous media at pore scales with wettability effects. The present method can handle large density and viscosity ratios, pertinent to many practical problems. As a practical application, we study multiphase flow in a micromodel representative of CO₂ invading a water-saturated porous medium at reservoir conditions, both numerically and experimentally. We focus on two flow cases with (i) a crossover from capillary fingering to viscous fingering at a relatively small capillary number, and (ii) viscous fingering at a relatively moderate capillary number. Qualitative and quantitative comparisons are made between numerical results and experimental data for temporal and spatial CO₂ saturation profiles, and good agreement is found. In particular, a correlation analysis shows that any differences between simulations and results are comparable to intra-experimental differences from replicate experiments. A key conclusion of this work is that system behavior is highly sensitive to boundary conditions, particularly inlet and outlet ones. We finish with a discussion on small-scale flow features, such as the emergence of strong recirculation zones as well as flow in which the residual phase is trapped, including a close look at the detailed formation of a water cone. Overall, the proposed model yields useful information, such as the spatiotemporal evolution of the CO₂ front and instantaneous velocity fields, which are valuable for understanding the mechanisms of CO₂ infiltration at the pore scale.

© 2018 Elsevier Ltd. All rights reserved.

1. Introduction

The sequestration of carbon dioxide (CO₂) in geological reservoirs is considered by many to be an essential component in the effective reduction of carbon emissions to the atmosphere, and therefore a critical tool in the battle against global climate change (Huppert and Neufeld, 2014; Pacala and Socolow, 2004). Among possible sites, deep saline aquifers are of particular interest owing to their large potential storage capacity, worldwide availability, and minimal environmental impact (Bachu, 2000; Gunter et al., 1997; Koide et al., 1992). Central to this approach is accurately predicting both the fidelity of candidate storage sites during pre-injection of CO₂ and its migration post-injection, which is complicated by multiple factors. Most notably, under typical reservoir conditions, CO₂ is less dense and less viscous than the resident brine which poten-

tially leads to complex and unstable displacement patterns as the CO₂ infiltrates the pore space both during and after injection. Complex patterns that emerge at the pore scale lead to macroscopic behaviors that are difficult to predict using current theories. Recent observations reveal that the macroscopic dynamics of the interface front is strongly tied to, and often controlled by, a range of pore-scale phenomena, such as fingering and Haines jumps (Lenormand et al., 1988; Moebius and Or, 2014). It is also increasingly accepted that developing subgrid-scale models capable of accurately representing pore-scale processes is a prerequisite to improving the performance of reservoir-scale simulations, yet the multiphase, multiphysics, and multiscale nature of the flow make this task inherently challenging. Therefore, a fundamental understanding of dynamic displacement processes at the pore scale is highly desirable.

Extensive experimental studies of multiphase flows in porous media have been performed using different approaches. A number of studies have attempted to observe pore-scale flows directly in three-dimensional (3D) porous models, or real rock samples, by employing x-ray micro computed tomography (micro-CT) and

* Corresponding author at: Department of Civil and Environmental Engineering and Earth Sciences, University of Notre Dame, Notre Dame, IN 46556, USA.

E-mail address: bolster@nd.edu (D. Bolster).

magnetic resonance imaging (MRI) (Andrew et al., 2014; Perrin and Benson, 2010). While these experiments explore the most realistic flows and geometries, due to a lack of optical access, expensive equipment (e.g., micro-CT and MRI) is a necessity. Moreover, these techniques are generally limited to low temporal resolution and are not best suited for acquiring temporally-resolved data, which is crucial for studying *dynamic* displacement processes. On the other end of the spectrum, more idealized 2D porous media, or so-called micromodels, have been used extensively to study multiphase flows at the pore scale (Armstrong and Berg, 2013; Blois et al., 2015; Chen et al., 2017; Karadimitriou et al., 2014; Kazemifar et al., 2015; 2016; Li et al., 2017; Roman et al., 2016; Zhang et al., 2011a; 2011b). In these micromodels, carefully designed or reprinted 2D patterns are etched in silicon or glass slides, to which a glass slide is bonded to form a closed cell. These 2D micromodels enable direct observation and measurement of pore-scale displacement processes using fluorescent microscopy or more advanced techniques, such as microscopic particle image velocimetry (micro-PIV) (Kazemifar et al., 2015; 2016; Li et al., 2017; Roman et al., 2016). Such 2D micromodels have served as excellent tools for studying the fundamental physics of pore-scale flows in porous media. The experimental data generated in such studies also provide a convenient basis for the validation of numerical and theoretical models. Although there is great value to this, the highly sensitive and unstable nature of multiphase flows makes direct quantitative comparison between experimental data and simulations challenging as it is virtually impossible to exactly match boundary and initial conditions. One must consider this carefully when evaluating the success or failure of a numerical approach as benchmarked against experiments (Ferrari et al., 2015).

Complementary to experiments, numerical simulations can provide access to further and more detailed information about the flow field, particularly at the pore scale (Lenormand et al., 1988), thereby complementing experimental studies in many ways. Existing numerical techniques for studying fluid flow through porous media are manifold, e.g., pore-network modeling (Blunt and King, 1991), smoothed-particle hydrodynamics (SPH) (Tartakovsky and Meakin, 2006), and lattice-Boltzmann method (LBM) (Huang et al., 2015), among others. Here we focus on LBM, which is popular due to its (a) mesoscopic nature, (b) strength in dealing with complex geometries, and (c) ease of parallelization with good scalability on distributed-memory machines.

In addition to the pseudo-potential LB model (Martys and Chen, 1996; Porter et al., 2009; Shan and Chen, 1993), perhaps the most common LB model for simulating multiphase flow in porous media is the color-gradient, or chromodynamic, model (Ba et al., 2016; Gunstensen et al., 1991; Huang et al., 2014; Leclaire et al., 2015), with which it is relatively easy to implement different wettability conditions at solid surfaces, and which scales well for parallel computations. While having many advantages, this simplicity also comes at a cost. Strictly speaking, the color-model is limited to density-matched fluids and numerical stability issues arise for large viscosity ratios and/or small capillary numbers. Although progress has been made in achieving high density ratios (Ba et al., 2016) and in reducing spurious velocities by adding correction terms (Leclaire et al., 2015), the resulting formulations impede computational efficiency and parallelism of the color-gradient model, making these schemes less practical for efficient simulation of CO₂ infiltration into water-saturated homogeneous and heterogeneous porous media with realistic density or viscosity ratios (Chen et al., 2017; Liu et al., 2015; 2014).

Phase-field LB models are an alternative framework, with which one can alleviate some of the aforementioned issues (Fakhari and Rahimian, 2010). Most of the available phase-field models are based on the Cahn–Hilliard equation, which requires the calculation of a fourth-order derivative; this, however, can be cumbersome

and problematic in terms of accuracy, efficiency, and stability (Geier et al., 2015). Additionally, while some studies exist that implement arbitrary contact angles within Cahn–Hilliard-based LB models (Connington and Lee, 2013), these are complicated to implement and the accuracy of implementing the wettability condition is questionable (Connington et al., 2015). An alternative to this is the conservative phase field LBM (Geier et al., 2015), which does not require the calculation of a fourth-order derivative and has other advantages over the Cahn–Hilliard equation (Geier et al., 2015). Recently, we proposed such a conservative phase-field LBM for numerical modeling of contact line dynamics on curved boundaries in multiphase flows (Fakhari and Bolster, 2017). We have also examined the accuracy and reliability of several phase-field LB schemes (Fakhari et al., 2017b). Here, we further develop the phase-field LBM (Fakhari and Bolster, 2017) with wettability effects for heterogeneous solid structures with realistic CO₂-brine density and viscosity ratios, which is currently not possible using the color-gradient model. We apply this framework to conduct numerical experiments on CO₂ invasion into a water-saturated porous micromodel for two select capillary numbers, representative of capillary and viscous fingering. We concurrently carry out matching experiments, to which our numerical simulations are both qualitatively and quantitatively compared.

Details of the experimental setup, apparatus, and methods are given in Section 2. The phase-field LBM and its numerical implementation details are presented in Section 3. A thorough comparison between numerical findings and experimental data is provided in Section 4. Discussion of numerical and experimental results is presented in Section 5, followed by a summary and conclusions in Section 6.

2. Experiment design

2.1. Micromodel

The micromodels used in this study were fabricated from a silicon wafer using micro-fabrication techniques (Chomsurin and Werth, 2003; Kazemifar et al., 2015). They consist of a heterogeneous porous section, an inlet, and an outlet, as shown in Fig. 1. The unique aspect of the fabricated micromodel is that the porous section represents the pore structure of real sandstone based on a previous study (Zuo et al., 2013). To generate the geometry, the pattern encoded in a binary image (provided by Zuo et al., 2013) was first generated from a micro-CT scan of a thin slice of sandstone. Due to limited connectivity associated with the 2D nature of the image, the pattern was slightly modified to enlarge the throat size and thus reduce the likelihood of flow blockages. The average and minimum throat sizes are 48 μm and 12 μm, respectively. The full porous section is made up by repeating the basic unit pattern in a 3 × 3 matrix, which has dimensions of $(L_x, L_y, L_z) = (7.101, 5.328, 0.030)$ mm and a porosity of $\varepsilon = 0.495$. Based on the pattern matrix, sequential processes involving standard photolithography, inductively coupled plasma-deep reactive ion etching (ICP-DRIE), diamond drilling, thermal oxidation, and anodic bonding were used to create the heterogeneous structures and to form a 2D micromodel. It is worth noting that, after thermal oxidation, 100 nm of silicon dioxide was grown on the silicon wafer, which rendered the surface just as hydrophilic as the glass wafer, to which the silicon wafer was bonded to form a closed flow cell. The contact angle of water on both surfaces was estimated to be $\sim 9 \pm 1$ degrees using CO₂ as the non-wetting phase. The contact angle was measured on flat glass and silicon samples under actual experimental conditions (80 bar, 21 °C), using a separate setup. The samples for contact angle measurement were prepared using the same oxidizing and cleaning procedures as for making the micromodel. In addition, during the course of each experiment,

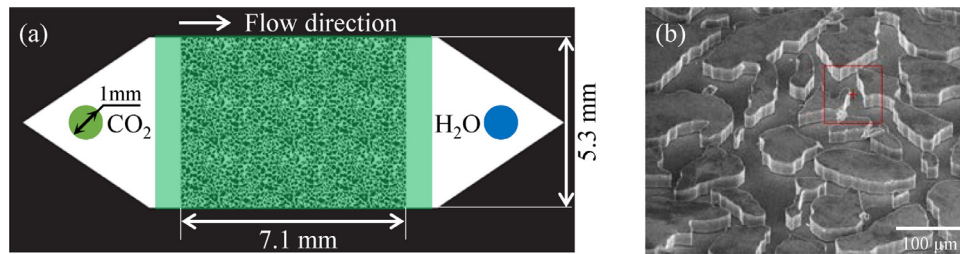


Fig. 1. (a) Schematic diagram of the micromodel with the imaging field of view noted in green. (b) A scanning electron microscope (SEM) image of a portion of the porous section within a typical micromodel. Note the depth of the micromodel (perpendicular to the plane) is 30 μm . (For interpretation of the references to colour in this figure legend, the reader is referred to the web version of this article.)

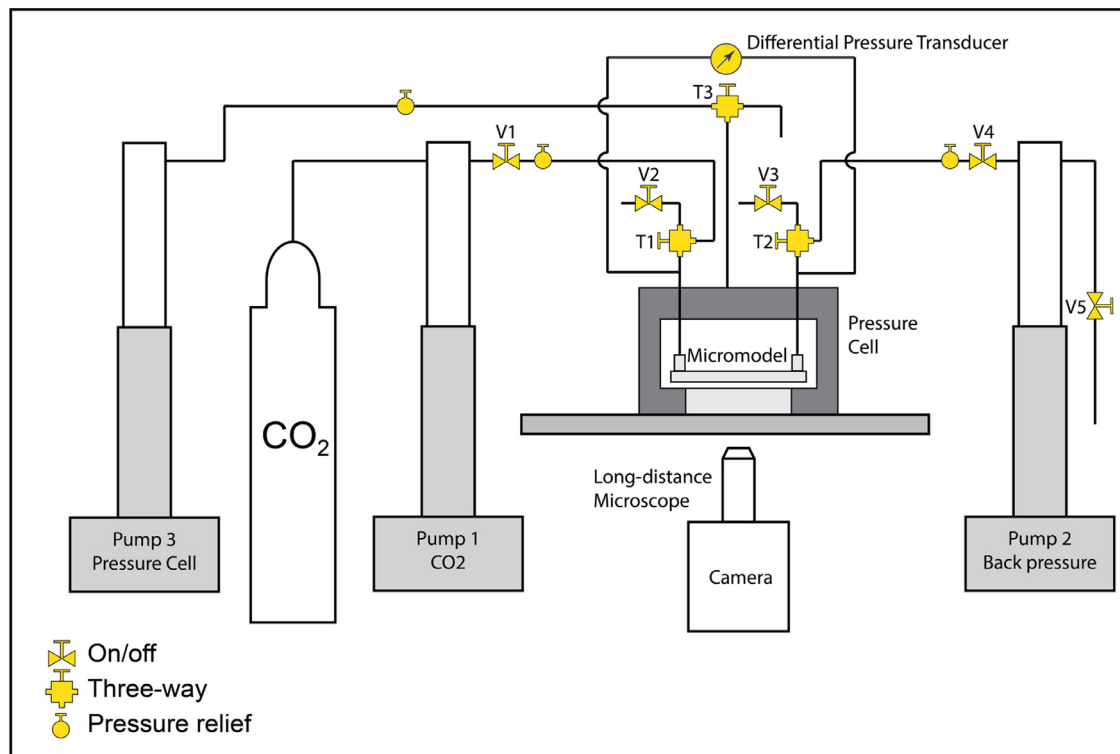


Fig. 2. Schematic diagram of the flow system, with pump 1 pushing the liquid CO_2 , pump 2 withdrawing water, and pump 3 controlling the pressure in the overburden pressure cell. The differential pressure transducer and the camera record the pressure drop across and the invasion pattern within the micromodel, respectively.

we performed an in-situ contact angle measurement using fluorescent microscopy in the triangular area near the inlet. Both measurement approaches yielded consistent measures of the contact angle. Two nanoports (IDEX Health & Science) were attached to the micromodel for fluid delivery.

2.2. Experimental setup and procedure

The coupled flow of water and CO_2 through the micromodel was controlled by two high-pressure syringe pumps (Teledyne Isco 100DM), as shown schematically in Fig. 2. Pump 1, filled with liquid CO_2 , was connected to the inlet (left port) of the micromodel and was used to push liquid CO_2 . Pump 2, filled with distilled water, was connected to the outlet (right port) to withdraw water. This approach allowed accurate maintenance of the back pressure of the flow system while achieving a constant volumetric flow rate. In order to protect the micromodel from over-pressurization, the micromodel was placed within an overburden pressure cell, whose pressure was controlled by a third high-pressure syringe pump (pump 3, Teledyne Isco 500D) and always maintained at least 5 bar above the micromodel pressure throughout the experiment. The overburden pressure cell is simply a cavity made of stainless steel

with a sapphire viewing window built into its base, whose sole purpose is to maintain the structural integrity of the micromodel during experiments at reservoir-relevant pressures. The pressurization procedures were as follows: before connecting Valve T1 to the pressure cell, the micromodel was pre-saturated with water using pump 2 from right to left. Then, valve T1 was connected to the pressure cell and the micromodel, and switched to the line of V1. Since valves V1, V2, V3, and V5 were all closed, with V4 open, the micromodel and pump 2 essentially form a closed internal space, whose pressure can be increased by simply running pump 2 in the forward direction. At this point, pump 3 and pump 2 were run simultaneously until pressures of 86 bar and 80 bar, respectively, were achieved. A high-speed differential pressure transducer (Validyne, P55E-1-N-2-42-S-5-A, 0–140 kPa, 0.1% accuracy) was used to measure the instantaneous pressure drop across the micromodel.

Prior to each experiment, the CO_2 was tagged with the fluorescent dye Coumarin 153, following Zhang et al. (2011b). The CO_2 pump was then pressurized to 80 bar and allowed to equilibrate at room temperature for over 2 hr. Meanwhile, the micromodel was mounted in the overburden pressure cell, which was then filled with glycerol to facilitate pressurization. To begin the experiment,

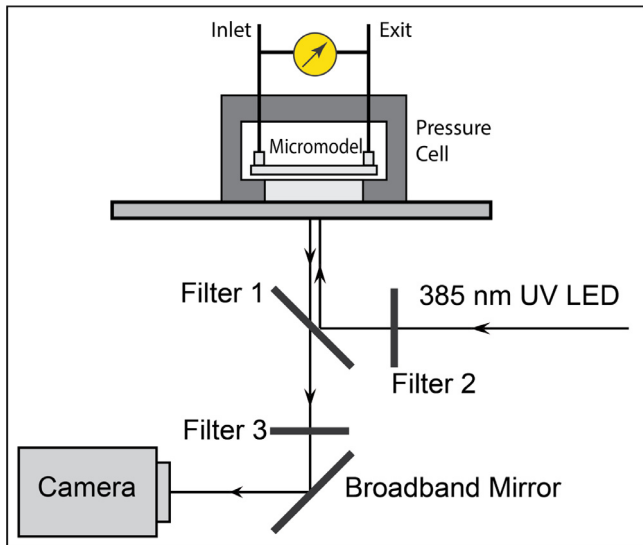


Fig. 3. Schematic diagram of the optical setup illustrating the epi-fluorescence microscopy technique employed. The 385 nm UV LED serves as the illumination source to excite fluorescence from the Coumarin 153 dye in the CO₂ phase.

the micromodel was pre-saturated with pure distilled water under ambient conditions through the outlet. The micromodel and the pressure cell were then pressurized simultaneously to 80 and 86 bar, respectively. After the pressures on the water side and CO₂ side both reached equilibrium, the valve V1 on the CO₂ line was opened and the CO₂ and water pumps were simultaneously initiated to run at the desired volumetric flow rates, each with an accuracy of 0.3% of the setpoint.

The instantaneous phase configuration as CO₂ infiltrated into the water-saturated micromodel was imaged using the epi-fluorescence microscopy technique, as illustrated in Fig. 3. An LED light source (Thorlabs M385LP1) with a nominal wavelength of 385 nm and a full width at half maximum of 12 nm filtered by a bandpass filter (Filter 2; Semrock BrightLine FF01-379/34-25) was used to excite the Coumarin 153 dye marking the CO₂ phase. The fluorescence emitted from the dye was passed through a dichroic mirror and a $\lambda = 445 \pm 20$ nm bandpass filter (Filter 3; Semrock BrightLine FF01-445/40-25), and focused by a long-distance microscope objective (Infinity Photo-Optical Company, K2 DistaMax) onto the detector of a 4 mega-pixel, 12-bit, high-speed CMOS camera (Phantom v641). With this imaging setup, the resultant magnification and spatial resolution were 2.9 and 3.4 μm , respectively, and the field of view was approximately 8.8 mm by 5.5 mm, which was sufficient to cover the entire porous section of the micromodel (as indicated by the green region in Fig. 1). Gray-scale images were captured at 1000 Hz in order to temporally resolve the dynamic flow processes. Owing to the epi-fluorescence configuration, the signal-to-noise ratio (intensity of CO₂ versus intensity of water or solid matrix) of the acquired images was typically greater than 5, which allowed for an unambiguous determination of the instantaneous CO₂ distribution in each image. The saturation of CO₂ in each frame was calculated by simply thresholding the gray-scale image and counting the pixels occupied by CO₂. Due to the non-uniformity of the illumination resulting from imperfections of collimating optics, the pixels in the center of an image appeared slightly brighter than those on the edges. In order to account for this effect, a dynamic thresholding scheme was applied, i.e. we divided our image into sub-regions within which we calculated the local maximum and minimum intensities; a threshold for the sub-region was determined based on these two intensities. This method was validated with a separate experiment in

Table 1

Physical properties of CO₂ and water at reservoir conditions (8 MPa and 21°C) (Linstrom and G, 2001).

ρ_c [kg/m ³]	ρ_w [kg/m ³]	μ_c [kg/m.s]	μ_w [kg/m.s]	σ [kg/s ²]
818.55	1001.6	7.40×10^{-5}	9.75×10^{-4}	0.0294

a micromodel saturated with dyed methanol, and the calculated porosity and the design value differed by less than 3%. Since the same set of image processing procedures with identical parameters was used in the validation experiment, as well as in all actual measurements, we consider 3% to be an accurate representation of the relative error of the measurements presented herein. Additional details of this experimental approach can be found in Ref. Kazemifar et al. (2015).

The physics of the multiphase flow of CO₂ into a water-saturated porous micromodel can be characterized by four dimensionless groups: (i) The density ratio, $\rho^* = \rho_c / \rho_w$, where ρ_c and ρ_w are the densities of liquid CO₂ and water, respectively; (ii) the viscosity ratio, $\mu^* = \mu_c / \mu_w$, where μ_c and μ_w are the viscosities of liquid CO₂ and water, respectively; (iii) the Reynolds number, $\text{Re}_c = \rho_c U L_y / \mu_c$, where U is the bulk velocity defined as $U = Q / A \varepsilon$ with Q and A being the volumetric flow rate and the frontal area of the micromodel perpendicular to the flow, respectively; and (iv) the capillary number, $\text{Ca} = \mu_c U / \sigma$, where σ is the surface tension coefficient between liquid CO₂ and water. The fluid properties and the dimensionless numbers for the two experimental conditions studied are given in Tables 1 and 2, respectively.

3. Numerical modeling

We employ a phase-field LBM (Fakhari and Bolster, 2017) to numerically simulate the experiments described in the previous section. Strengths of this model include: (1) Good accuracy; (2) an ability to handle large density and viscosity ratios; (3) an evolution equation for pressure that is consistent with multiphase flow dynamics; and (4) the capability to model pre-specified contact angles with smaller spurious velocities than the color-gradient or pseudo-potential models (Fakhari and Bolster, 2017).

3.1. Phase-field LBM

The proposed phase-field LBM is designed to solve the flow-field for isothermal, incompressible multiphase fluid systems, and consists of two main parts. The first is a lattice Boltzmann equation (LBE) for tracking the interface between two different fluids according to the so-called conservative phase-field equation (Chiu and Lin, 2011)

$$\frac{\partial \phi}{\partial t} + \nabla \cdot (\phi \mathbf{u}) = \nabla \cdot \left[M \left(\nabla \phi - \frac{4}{\xi} \phi (1 - \phi) \hat{\mathbf{n}} \right) \right] \quad (1)$$

where ϕ is the phase field, which is zero in the relatively light fluid (CO₂) and one in the relatively heavy fluid (water) and changes smoothly across the interface, t is time, \mathbf{u} is the macroscopic velocity vector, M is the mobility, ξ is the interfacial thickness, and $\hat{\mathbf{n}}$ is the unit vector normal to the (CO₂-water) interface

$$\hat{\mathbf{n}} = \frac{\nabla \phi}{|\nabla \phi + \epsilon|} \quad (2)$$

where $\epsilon = 10^{-32}$ is a small number to avoid division by zero. The last term in the parentheses in (1) is an anti-diffusion term that exists only within the interfacial region and prevents the interface from becoming excessively diffusive. For a detailed physical explanation please see Ref. Geier et al. (2015).

Table 2
Dimensionless groups for the case studies.

Flow rate (Q)	Ca	Re _c	ρ*	μ*	θ	log μ*	log Ca
0.05 [ml/min]	2.65 × 10 ⁻⁵	620.9	0.817	0.076	9°	-1.12	-4.58
0.25 [ml/min]	1.33 × 10 ⁻⁴	3104.7	0.817	0.076	9°	-1.12	-3.88

In phase-field modeling, the volumetric free energy of the system is given by Jacqmin (1999, 2000)

$$\mathcal{F} = \oint \left(\beta \Psi(\phi) + \frac{1}{2} \kappa |\nabla \phi|^2 \right) dV \quad (3)$$

where $\beta = 12\sigma/\xi$, $\kappa = 3\sigma\xi/2$, and the bulk free energy used in this study is

$$\Psi(\phi) = \phi^2(1 - \phi)^2 \quad (4)$$

The chemical potential of the system μ_ϕ is then found by minimizing the free energy according to

$$\mu_\phi = \frac{\delta \mathcal{F}}{\delta \phi} = 4\beta\phi(\phi - 1)(\phi - 1/2) - \kappa \nabla^2 \phi \quad (5)$$

where δ denotes the variational differentiation.

The second part of the proposed phase-field LBM is a pressure-evolution LBE for recovering the macroscopic equations, including conservation of mass,

$$\frac{\partial \rho}{\partial t} + \nabla \cdot \rho \mathbf{u} = 0 \quad (6)$$

and conservation of momentum (Navier–Stokes),

$$\rho \left(\frac{\partial \mathbf{u}}{\partial t} + \mathbf{u} \cdot \nabla \mathbf{u} \right) = -\nabla p + \nabla \cdot (\mu [\nabla \mathbf{u} + (\nabla \mathbf{u})^T]) + \mathbf{F}_s \quad (7)$$

where ρ and μ are the fluid density and viscosity, respectively, p is the macroscopic pressure, and $\mathbf{F}_s = \mu_\phi \nabla \phi$ is the surface tension force between different fluids.

Of note is that the main difference between the current phase-field LBM and that proposed in Ref. Fakhari and Rahimian (2010) is the interface-tracking equation. In particular, the Cahn–Hilliard equation is used in Ref. Fakhari and Rahimian (2010), while the current model is built upon the conservative phase-field equation (Geier et al., 2015). The current phase-field LBM, however, is identical to that proposed in Ref. Fakhari and Bolster (2017), with the additional contribution of implementing the wettability condition (a given contact angle) on a heterogeneous solid substrate, as will be described in Section 3.3.

3.1.1. LBE for interface tracking

We use the following LBE for tracking the interface between liquid CO₂ and water (Fakhari and Bolster, 2017):

$$h_\alpha(\mathbf{x} + \mathbf{e}_\alpha \delta t, t + \delta t) = h_\alpha(\mathbf{x}, t) - \frac{h_\alpha(\mathbf{x}, t) - h_\alpha^{\text{eq}}(\mathbf{x}, t)}{\tau_\phi + 1/2}, \quad (8)$$

where h_α is the phase-field distribution function, τ_ϕ is the phase-field relaxation time, \mathbf{e}_α is the lattice-dependent mesoscopic velocity set (He and Luo, 1997), and the equilibrium phase-field distribution function is

$$h_\alpha^{\text{eq}} = \phi \Gamma_\alpha + w_\alpha \frac{M}{c_s^2} \left[\frac{4}{\xi} \phi(1 - \phi) \right] (\mathbf{e}_\alpha \cdot \hat{\mathbf{n}}) \quad (9)$$

where

$$\Gamma_\alpha = w_\alpha \left[1 + \frac{\mathbf{e}_\alpha \cdot \mathbf{u}}{c_s^2} + \frac{(\mathbf{e}_\alpha \cdot \mathbf{u})^2}{2c_s^4} - \frac{\mathbf{u} \cdot \mathbf{u}}{2c_s^2} \right] \quad (10)$$

in which w_α is the lattice-dependent weight coefficient set (He and Luo, 1997), $c_s = c/\sqrt{3}$ is the speed of sound in the system with $c = \delta x/\delta t = 1$ lu (lattice units), where δx and δt are the lattice length

scale and time scale, respectively. The mobility is related to the phase-field relaxation time, τ_ϕ , by

$$M = \tau_\phi c_s^2 \delta t \quad (11)$$

Assuming a two-step collision-streaming sequence, the phase field is calculated by taking the zero-th moment of the phase-field distribution function after the streaming

$$\phi = \sum_\alpha h_\alpha \quad (12)$$

and then the density is updated by

$$\rho = \rho_W + \phi(\rho_W - \rho_C) \quad (13)$$

3.1.2. LBE for hydrodynamics

The following LBE is solved for recovering the hydrodynamic properties in nearly incompressible multiphase flows (Fakhari and Bolster, 2017)

$$\bar{g}_\alpha(\mathbf{x} + \mathbf{e}_\alpha \delta t, t + \delta t) = \bar{g}_\alpha(\mathbf{x}, t) + \Omega_\alpha(\mathbf{x}, t) + F_\alpha(\mathbf{x}, t) \quad (14)$$

where \bar{g}_α is the modified hydrodynamic distribution function, Ω_α is the collision operator, and F_α is

$$F_\alpha(\mathbf{x}, t) = \delta t \left[(\Gamma_\alpha - w_\alpha)(\rho_W - \rho_C) c_s^2 + \Gamma_\alpha \mu_\phi \right] (\mathbf{e}_\alpha - \mathbf{u}) \cdot \nabla \phi \quad (15)$$

We use the multiple-relaxation time (MRT) collision operator (Fakhari and Lee, 2013; Lallemand and Luo, 2000)

$$\Omega_\alpha(\mathbf{x}, t) = -\mathbf{M}^{-1} \hat{\mathbf{S}} \mathbf{M} (\bar{g}_\alpha - \bar{g}_\alpha^{\text{eq}}) \quad (16)$$

where \mathbf{M} is the orthogonal transformation matrix, $\hat{\mathbf{S}}$ is the diagonal relaxation matrix, and the modified equilibrium distribution function is

$$\bar{g}_\alpha^{\text{eq}} = g_\alpha^{\text{eq}} - \frac{1}{2} F_\alpha \quad (17)$$

in which

$$g_\alpha^{\text{eq}} = p w_\alpha + \rho c_s^2 (\Gamma_\alpha - w_\alpha) \quad (18)$$

is the equilibrium distribution function. The orthogonal transformation matrix is given in Ref. Lallemand and Luo (2000) for the D2Q9 lattice used in the present study.

In order to update the (hydrodynamic) relaxation time, we first calculate the dynamic viscosity according to

$$\mu = \mu_C + \phi(\mu_W - \mu_C) \quad (19)$$

followed by updating the relaxation time according to

$$\tau = \frac{\mu}{\rho c_s^2} \quad (20)$$

This approach has been shown to be more accurate than directly calculating the relaxation time from the phase field using a linear or harmonic interpolation (Fakhari et al., 2017b).

After solving the LBE (14) using a routine collision-streaming sequence, the hydrodynamic properties are calculated by

$$\mathbf{u} = \frac{1}{\rho c_s^2} \sum_\alpha \bar{g}_\alpha \mathbf{e}_\alpha + \frac{\delta t}{2\rho} \mathbf{F}_s \quad (21a)$$

$$p = \sum_\alpha \bar{g}_\alpha + \frac{\delta t}{2} (\rho_W - \rho_C) c_s^2 \mathbf{u} \cdot \nabla \phi \quad (21b)$$

Note that the updated velocity is used in calculation of the pressure.

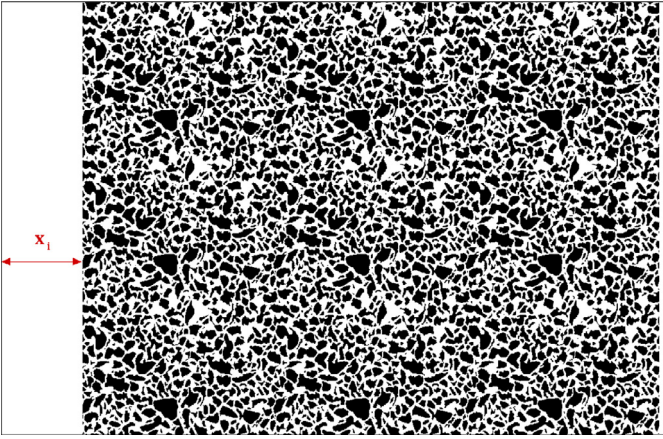


Fig. 4. The computational domain containing the same heterogeneous porous matrix as the experiments. Here, x_i is the distance from the inlet boundary, where the liquid CO₂ front is located, to the beginning of the porous section.

3.2. Numerical implementation

To implement the LBM described in the previous section, one must be able to calculate the gradients of the phase field. For mass balance and stability reasons this is done using second-order, isotropic differences (Fakhari and Bolster, 2017). Although one might lose accuracy at high density ratios, using central differences has shown to be very effective and reasonably accurate for numerical simulation of multiphase flows at low density ratios, which is the case in the present study.

The numerical values of mobility M and interfacial thickness ξ play a key role in the stability and accuracy of phase-field LB models. The effects of these numerical parameters on the simulation results was considered by Fakhari et al. (2017a), who conducted a sensitivity analysis. Here we use the empirical guidelines described in Ref. Fakhari et al. (2017a) to choose these parameters. In general, having a small ξ is desirable, as this improves convergence towards sharp-interface solution. A small value for ξ , however, might lead to numerical instability, especially at high density ratios. As suggested in Ref. Fakhari et al. (2017a), we use $\xi = 3$ lu, which is an optimal value for interfacial thickness at low density ratios (less than 10). Similarly, a high value for the mobility results in excessive numerical dissipation, which deteriorates the accuracy of the results. On the other hand, having a too small M might cause numerical instability. In this work, we set the mobility to $M = 0.01$ lu (Fakhari et al., 2017a).

The computational domain, shown in Fig. 4, is discretized using 2131×1599 grid cells. On the left boundary, where a flat CO₂ front is located, we impose a parabolic (Poiseuille) profile as the inlet velocity, while a convective outflow boundary condition (BC) is applied on the right boundary. As will be shown in Section 4.1, the distance from the inlet to the porous section of the micromodel (x_i) has a noticeable effect on the numerical results. The bottom and top boundaries are treated as solid walls with wettability conditions (more on this in Section 3.3). We represent the solid grains using stair-shaped boundaries. Boundary conditions are imposed using bounce-back on the link to find the value of the unknown distribution functions coming from the solid cells towards the fluid domain. Details of implementation of the initial and boundary conditions, as well as enforcement of an arbitrary contact angle on solid walls, are described below.

3.3. Wettability condition on solid boundaries

Implementing wettability conditions is easily done in, for example, the color-gradient and pseudopotential LB models, because there is no need to calculate the vector normal to the solid boundary in those models. This, however, comes with some drawbacks, such as large spurious velocities and restriction to density-matched fluids. On the other hand, finding the normal to the solid surface in a heterogeneous solid structure can be cumbersome in phase-field models. To the best of our knowledge, there are few studies for implementing arbitrary contact angles in Cahn–Hilliard-based LB models (Connington and Lee, 2013). Aside from a complicated algorithm and tedious implementation, the accuracy of implementing the wettability condition is questionable (Connington et al., 2015). Although contact line dynamics on (homogeneous) curved solid boundaries have been recently proposed (Fakhari and Bolster, 2017), there is no contact angle treatment for heterogeneous solid structures in conservative phase-field models. For this purpose, we present a straightforward algorithm here.

To impose a pre-specified contact angle at the solid walls, the wall free energy is postulated to be of the form (Ding and Spelt, 2007; Jacqmin, 2000)

$$\kappa \hat{\mathbf{n}}_w \cdot \nabla \phi|_{\mathbf{x}_w} = -6\sigma \sqrt{\Psi(\phi)} \cos \theta \quad (22)$$

which can be simplified to (Fakhari and Bolster, 2017)

$$\hat{\mathbf{n}}_w \cdot \nabla \phi|_{\mathbf{x}_w} = -\sqrt{\frac{2\beta}{\kappa}} \phi_w (1 - \phi_w) \cos \theta, \quad (23)$$

where $\hat{\mathbf{n}}_w$ is the unit vector out-normal to the solid wall, θ is the static contact angle, and ϕ_w is the (unknown) value of the phase field at the wall. The unknown quantities in Eq. (23) are $\hat{\mathbf{n}}_w$ and ϕ_w . The out-normal vector, $\mathbf{n}_w = (n_x \hat{\mathbf{x}}, n_y \hat{\mathbf{y}})$, depends on the given geometry. For stationary boundaries, which is the case in the present study, it can be readily calculated a single time at the beginning of the simulations. Referring to Fig. 5(a), boundary cells (marked as red circles) can be easily identified by those solid cells that have at least one neighboring fluid cell. Once the boundary cells are identified, their out-normal vectors can be determined by probing the adjacent boundary cells. For a 2D geometry, we find the x and y components of the normal vector according to the following algorithm: if both left and right neighbors of a given boundary cell are solid cells, then the normal vector is in the y -direction ($n_x = 0$); otherwise, n_x points in the x -direction where there is a fluid cell. Similarly, if both bottom and top neighbors are solid walls, the normal vector is in the x -direction ($n_y = 0$); otherwise, n_y points to an available fluid cell in the y -direction. If all orthogonal (bottom, top, left, and right) neighbors are solid cells, then we pick the first diagonal neighbor that is a fluid cell and define the normal vector accordingly. This process takes care of the majority of boundary cells with only few exceptions, such as convex corner nodes, which will be handled separately to make sure that the normal vector is consistently pointing to a fluid cell.

After finding the vectors normal to the boundary cells, we can eliminate ϕ_w in Eq. (23) using the following relations

$$\hat{\mathbf{n}}_w \cdot \nabla \phi|_{\mathbf{x}_w} = \frac{\partial \phi}{\partial n_w} \Big|_{\mathbf{x}_w} = \frac{\phi_f - \phi_s}{2h} \quad (24a)$$

$$\phi_w = \frac{\phi_f + \phi_s}{2} \quad (24b)$$

where $\mathbf{x}_f = \mathbf{x}_s + \mathbf{n}_w$, $\phi_f = \phi(\mathbf{x}_f)$, $\phi_s = \phi(\mathbf{x}_s)$, and $2h = |\mathbf{x}_f - \mathbf{x}_s| = |\mathbf{n}_w|$ is the distance between the boundary cell and the fluid cell (in the orthogonal directions $2h = 1$ lu, while in the diagonal directions $2h = \sqrt{2}$ lu). Substituting Eq. (24) into Eq. (23) then gives

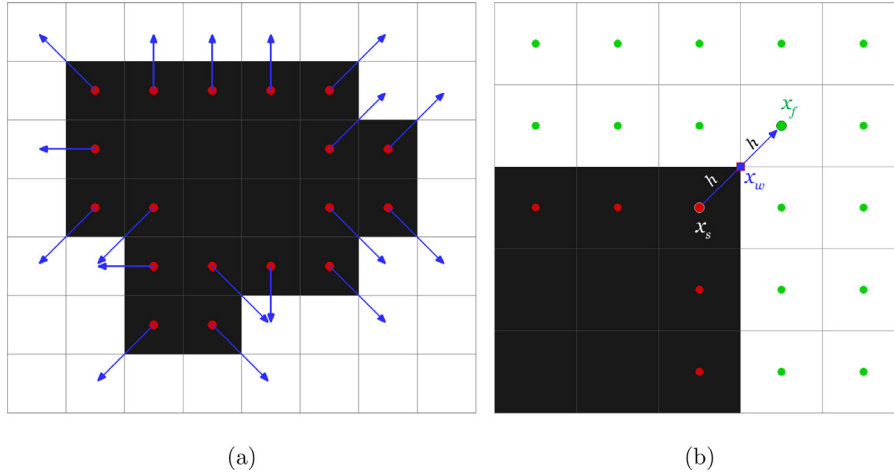


Fig. 5. Typical solid substrates. (a) schematic of normal vectors \mathbf{n}_w ; (b) solid boundary nodes and fluid nodes. The normal vectors are shown by blue lines, boundary-cell centers are shown by red circles, and fluid-cell centers are shown by green circles. (For interpretation of the references to colour in this figure legend, the reader is referred to the web version of this article.)

us the unknown value of the phase field at the boundary cells:

$$\phi_s = \frac{1}{a} \left(1 + a - \sqrt{(1+a)^2 - 4a\phi_f} \right) - \phi_f \quad (25)$$

where

$$a = -h \sqrt{\frac{2\beta}{\kappa}} \cos \theta \quad (\theta \neq 90^\circ) \quad (26)$$

For neutral wetting conditions ($\theta = 90^\circ$) the trivial solution is $\phi_s = \phi_f$.

3.4. Boundary conditions for the distribution functions

In addition to the wetting BC for the phase field at the solid walls, the distribution functions coming from the boundary nodes towards the fluid nodes must be determined. Noting the post-collision state of the distribution functions by f^* , where f is a placeholder for either h or \bar{g} , the value of f_i^* at a typical solid boundary node (\mathbf{x}_s) is unknown. Referring to Fig. 5(b), we use the mid-way bounce-back rule to determine the unknown distribution functions at the boundary nodes before the streaming step,

$$f_j^*(\mathbf{x}_s) = f_i^*(\mathbf{x}_f) \quad (27)$$

where j denotes the bounce-back direction such that $\mathbf{e}_j = -\mathbf{e}_i$. Given a predetermined, stationary geometry, we identify each boundary node and store its coordinates (using two integer numbers) together with two indices to identify its normal direction.

3.5. Initial, inlet, and outlet boundary conditions

Initially, the porous medium is saturated with water, and the phase field is initialized according to

$$\phi(x, y) = \frac{1}{2} \left[1 + \tanh \left(\frac{x - \xi}{\xi/2} \right) \right] \quad (28)$$

In other words, at the initial time, the CO_2 front is a flat interface located at $x = \xi$. A parabolic velocity profile is imposed at the inlet using the non-equilibrium bounce-back scheme (Zou and He, 1997) after the streaming step, according to

$$f_i|_{x=0} = (f_o + f_i^{eq} - f_o^{eq})|_{x=0} \quad (29)$$

where f is a placeholder for h or \bar{g} , and the subscripts i and o denote the incoming and outgoing distribution functions, respectively, such that $\mathbf{e}_o = -\mathbf{e}_i$. The outgoing distribution functions (f_o)

are known after the streaming step, and the equilibrium values (f_i^{eq} and f_o^{eq}) are found via Eqs. (9) and (17) by imposing a uniform phase field ($\phi = 0$) and a parabolic velocity profile at the inlet.

At the outlet, we impose the following convective outflow BC for the unknown distribution functions entering the domain

$$\frac{\partial f_i}{\partial t} + u_c \frac{\partial f_i}{\partial x} \Big|_{x=x_o} = 0 \quad (30)$$

where x_o is the x -location of the outlet boundary, u_c is the convective velocity (to be specified) at the outlet. It is worth noting the key differences between the current convective BC and those presented in Ref. Lou et al. (2013). First, using the implicit upwind scheme, we solve Eq. (30) only for the unknown (incoming) distribution functions, while in Ref. Lou et al. (2013) Eq. (30) was solved for the distribution functions in all directions. Second, as opposed to a maximum, average, or local value for the outlet velocity in Ref. Lou et al. (2013), we propose to use the following convective velocity:

$$u_c(x_o, y) = \max\{0, u_x(x_o, y)\} \quad (31)$$

For consistency with the upwinding scheme, it is important to ensure that the convective velocity is positive. This is particularly crucial at small capillary numbers (or relatively low flow rates), where the characteristic velocity is comparable to spurious currents. In our simulations $U_0 \sim \mathcal{O}(10^{-4})$, which is too small for some common schemes to be numerically stable.

4. Results

In this section, results from both the LBM simulations and drainage experiments are shown, with both quantitative and qualitative comparisons made between them. To facilitate comparison, a dimensionless time was defined as $t^* = t/t_c$, where $t_c = L_x/U$ is the characteristic time with L_x being the length of the porous section. As listed in Table 2, two different flow rates, namely, 0.05 ml/min and 0.25 ml/min corresponding to capillary numbers of 2.65×10^{-5} and 1.33×10^{-4} , respectively, are studied at 8 MPa and 21°C. The cases with the low ($\log \text{Ca} = -4.58$) and the high ($\log \text{Ca} = -3.88$) flow rates are expected to fall within the crossover from capillary to viscous fingering and the viscous fingering regimes, respectively (Zhang et al., 2011b).

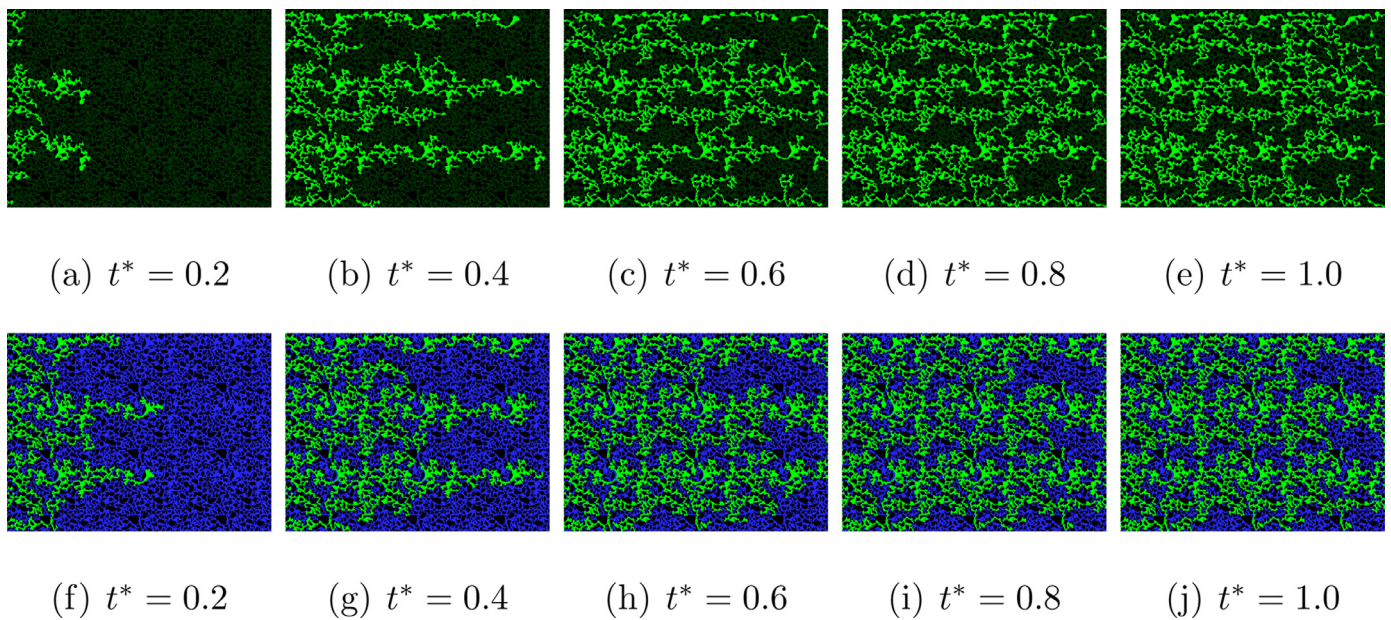


Fig. 6. CO₂ infiltration in the porous micromodel at $Ca = 2.65 \times 10^{-5}$. The top row shows experimental results, while the bottom row shows numerical simulations with $x_i = 5$ lu. Experimental results show the depth-averaged concentration, with the green representing the liquid CO₂ in both simulations and experiments, and the blue representing the resident water in the numerical simulations. (For interpretation of the references to colour in this figure legend, the reader is referred to the web version of this article.)

4.1. Crossover from capillary to viscous fingering ($Ca=2.65e-5$)

CO₂ infiltration into a water-saturated micromodel is a complicated process, involving the migration of the CO₂ front, the evolution of individual menisci, and the growth of dendritic structures (*i.e.* the fingers) (Kazemifar et al., 2016; Lenormand et al., 1988), as can be seen in the movies provided in the supplementary materials. Chronologically, the entire drainage process can be qualitatively classified into three distinct flow stages: (I) Migration of the CO₂ front in the triangular area (*c.f.*, Fig. 2), prior to its arrival at the porous section; (II) percolation of CO₂ through the micromodel, until the flow pattern within the porous section no longer changes (quasi-steady state); and (III) post-front passage, when the distribution of CO₂ and residual water remain largely unchanged for a long period of time. Note that during stage III, the flow pattern may eventually be altered by some very slow processes like CO₂ dissolution into water ganglia and shear-induced film flows (*i.e.* quasi-steady state) (Kazemifar et al., 2016; Li et al., 2017; Morais et al., 2016). However, these processes are so slow that they are beyond the time scales of interest in this work and, therefore, are not considered.

Fig. 6 shows a few representative snapshots of CO₂ infiltration into the water-saturated micromodel at different times for $Ca = 2.65 \times 10^{-5}$, including results from experiments and simulations (the full evolution can be seen in videos provided as supplementary materials). Here, $t^* = 0$ is chosen to correspond to the instant when the CO₂ front first reaches the porous section (*i.e.* when CO₂ saturation within the porous section first becomes non-zero). In the experiments, prior to $t^* = 0$, the CO₂ front propagates within the triangular region on the left of the porous section (*c.f.*, Fig. 1). The front remains significantly curved during this flow stage, meaning that the middle portion of the front arrives at the porous section much faster than it reaches the edges (see movies in supplementary materials). This middle portion of the CO₂ front becomes pinned to the solid substrate at the entrance of the porous section due to capillary resistance of the porous matrix, and the liquid CO₂ behind the front region continues to expand laterally towards the upper and lower boundaries of the mi-

cro-model. At $t^* = 0.2$, CO₂ partially breaks into the porous section in the form of fingers. It is evident that three primary fingers develop at locations corresponding to the most permeable pathways within the porous section, where capillary resistance is expected to be lower. These three fingers grow predominately in the horizontal direction from left to right, consistent with the direction of the bulk pressure gradient, thus displaying characteristics of viscous fingering (Zhang et al., 2011b). By $t^* = 0.4$, the three primary fingers have grown even further, nearly reaching the outlet boundary of the porous section. Besides these primary fingers, there are multiple secondary fingers that have formed between the primary ones, including side fingers emerging from each primary finger. The growth lines of these secondary and side fingers are not exactly aligned with the direction of the bulk pressure gradient, but rather occur in transverse directions and even backwards against the bulk pressure gradient, which is an indication of capillary fingering. The coexistence of patterns associated with capillary and viscous fingering suggest that this flow is in the crossover regime from capillary to viscous fingering, in agreement with previous flow phase diagram studies using homogeneous micromodels (Lenormand et al., 1988; Zhang et al., 2011b). At $t^* = 0.6$, while the primary fingers remain largely unchanged, the secondary and side fingers continue to grow, with each finger branching into multiple fingers in all directions. Another interesting feature of this snapshot (and in the following ones) is the existence of isolated CO₂ blobs within the porous section, presumably attributable to “snap-off” effects (Lenormand et al., 1983). These isolated blobs are observed in both the experiments and in the numerical simulations. At $t^* = 0.8$ and $t^* = 1.0$, the percolation process (stage II) is nearly complete, with all fingers nearly fully-developed. Although the spatial distributions of CO₂ and water remain largely unchanged during the rest of the experiment or simulation, it can be observed that at the ends of certain fingers, the CO₂ front can locally jump and/or retract over short distances, suggesting the existence of only a quasi-static system.

The results presented in Fig. 6 indicate fairly good qualitative agreement between the experiment and the 2D simulation, particularly considering the high complexity of the flow system

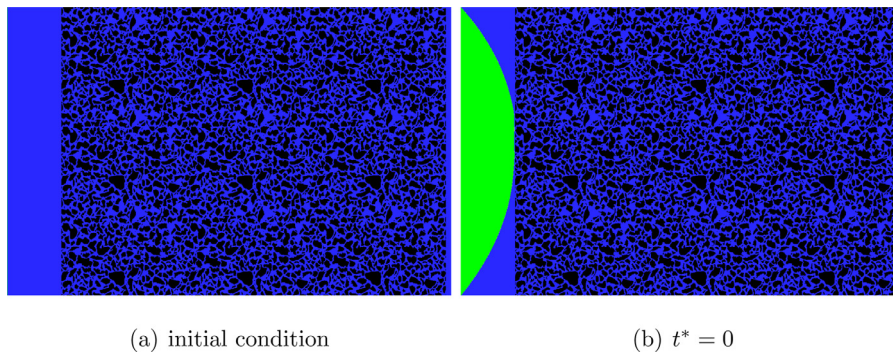


Fig. 7. The shape of the liquid CO₂ front when $x_i = 300$ lu. (a) The flat CO₂ front is placed at $x = \xi$ at the beginning of the simulations; (b) The liquid CO₂ front assumes a parabolic profile by the time it reaches the porous section of the micromodel at $t^* = 0$.

(i.e. unstable multiphase flow in a superhydrophilic, heterogeneous porous matrix). The simulation and experiment produce qualitatively similar dynamics of fingering, as well as similar spatial distributions of CO₂. Perhaps the most evident discrepancy between the experiment and simulation in Fig. 6 is that the development and advancement of the fingers in the simulations appears to be slightly ahead of that observed in the experiments. We conjecture that this difference can primarily be attributed to the discrepancy in the initial and boundary conditions between experiment and simulation, although of course model limitations and/or errors might also play a factor. As already noted, during flow stage I in the experiment, the CO₂ front is significantly curved within the triangular region, and the exact shape of the CO₂ front is not only difficult to control experimentally, but also difficult to match numerically. In fact, some discrepancies exist even between two trials of the same experiment (see Fig. 8). Moreover, the velocity field at the inlet boundary (for both the CO₂ and water sides) is significantly perturbed as a result of the propagation of the curved CO₂ front. Due to limitations of current measurement techniques (Kazemifar et al., 2015), the velocity field cannot be quantitatively evaluated in the CO₂ phase, and thus cannot be reconstructed and matched numerically.

Given that the liquid CO₂ pumps into the micromodel through a cylindrical tube in the experiments, we suspect that, numerically, placing a “flat” CO₂ front in the vicinity of the porous section will not accurately represent the experimental conditions. Upon careful inspection of the liquid CO₂ profile away from the porous region in the experiments, we observe a radial flow in the vicinity of the inlet tube (the green tube in Fig. 1), and, hence, a parabolic, rather than uniform, velocity profile close to the porous region (see the videos in supplementary materials). This behavior leads to a parabolic profile for the liquid CO₂ front at the entrance of the porous section. Thus, in order to better match the initial conditions between numerical simulations and experiment, we extended the length of the inlet region by two orders of magnitude, from $x_i = 5$ lu to $x_i = 300$ lu. After rerunning the simulations with $x_i = 300$ lu, we found that placing a flat CO₂ front close to the porous section of the micromodel is indeed erroneous (see the obtained parabolic CO₂ front in Fig. 7 when $x_i = 300$ lu).

A quantitative comparison of CO₂ saturation as a function of time, shown in Fig. 8 for $Ca = 2.65 \times 10^{-5}$, further confirm our speculation. Fig. 8, which depicts the data for two separate experiments (black circles and red squares) along with numerical simulations using two different entry lengths of $x_i = 5$ lu (green line) and $x_i = 300$ lu (blue line) shows an improvement in the temporal evolution of the CO₂ saturation in the porous micromodel when the length of the inlet region is increased to $x_i = 300$ lu.

As can be seen in Fig. 8, the shapes of the saturation curves are very similar between the experimental data and simulation results.

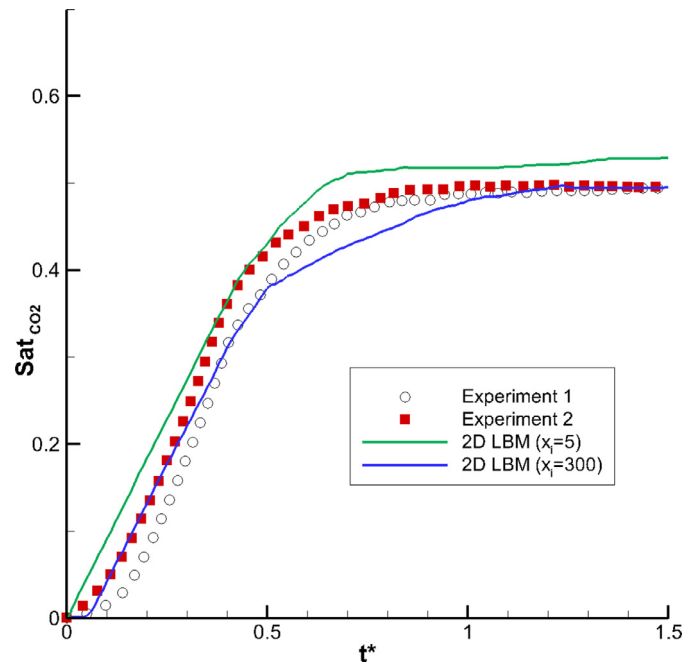


Fig. 8. Temporal variation of liquid CO₂ saturation: comparison between experiment and simulations for $Ca = 2.65 \times 10^{-5}$. The experiment was run twice, with the results from the first and second trials shown by black circles and red squares, respectively. Green line represents simulation data when the CO₂ front is placed 5 lattice cells from the inlet ($x_i = 5$ lu), and blue line represents simulation results when the CO₂ front is placed at $x_i = 300$ lu. (For interpretation of the references to colour in this figure legend, the reader is referred to the web version of this article.)

In particular, when the inlet region is extended to $x_i = 300$ lu, the new numerical results nearly match the experimental data, with the final CO₂ saturations (i.e. the quasi-steady state values) standing at 49.5%, 49.6%, and 49.5% for experiment 1, experiment 2, and simulation (blue line), respectively. These values represent a difference of less than 0.1% between the second experiment and the simulation, for which the CO₂ distributions are shown in Fig. 9 at $t^* = 1.5$. It is evident that the original simulation profile with $x_i = 5$ lu (green line) has a higher final saturation than the experimental data for most of the range of t^* shown in Fig. 8. This is consistent with the observation from Fig. 6 that the development of fingers in the original simulations is ahead of that in experiment, due to the different inlet boundary conditions.

In order to further compare the simulations with the micromodel experiments in a quantitative way, spatial profiles of CO₂ saturation in the porous micromodel are plotted in Fig. 10 at quasi-steady state ($t^* = 1.5$) for $Ca = 2.65 \times 10^{-5}$ for both experiments

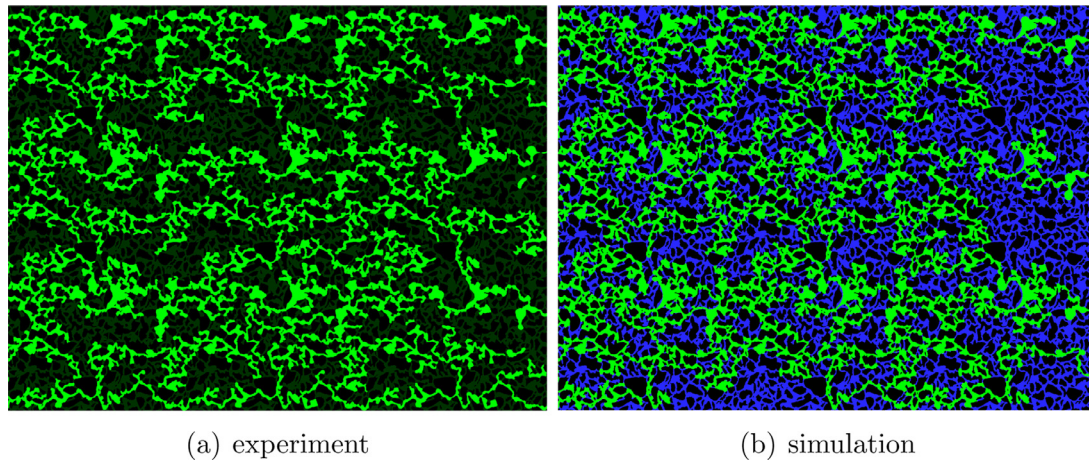


Fig. 9. Final CO_2 saturation in the porous micromodel for $\text{Ca} = 2.65 \times 10^{-5}$ at $t^* = 1.5$. (a) Second trial of experiments, and (b) numerical simulation with $x_i = 300$ lu.

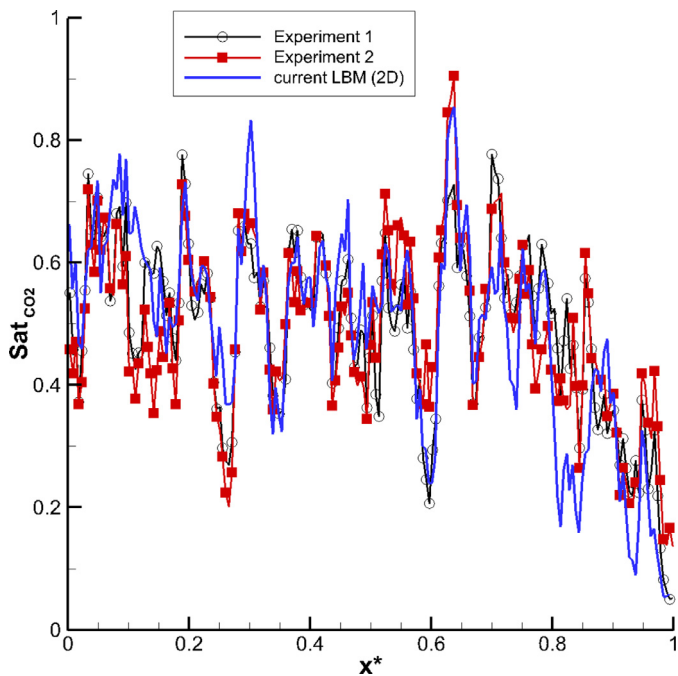


Fig. 10. The spatial variation of liquid CO_2 saturation inside the porous micromodel at quasi-steady state ($t^* = 1.5$) for $\text{Ca} = 2.65 \times 10^{-5}$. Saturation is obtained by averaging along the vertical y axis. Comparison between experiment and simulations with $x_i = 300$ lu. The experiments are attempted twice, with the results from the first and second trials shown with black and red lines with symbols, respectively. The simulation result is shown with a blue line. (For interpretation of the references to colour in this figure legend, the reader is referred to the web version of this article.)

and simulation. To calculate the data for the spatial profile using simulation results, the entire porous section (2131×1599 grid cells) was first divided into 194 bins (*i.e.* 193 bins each with a width of 11 grid cells and one last bin with a width of 8 grid cells) in the horizontal direction, and then the local CO_2 saturation was calculated within each bin by counting the cells filled with CO_2 . For the experimental data, the acquired image (with a typical size of 2066×1550 pixels) was first mapped onto a 2131 by 1599 matrix using bilinear interpolation, and then the local CO_2 saturation at each x -location was calculated following the same procedure as used in the simulations. As shown in Fig. 10, the spatial saturation profile obtained using LB simulation compares favorably with experimental data, predicting most of its peaks and valleys

with reasonable accuracy, although some discrepancies do exist. It must be noted though that even intra-experimental variability exists and that the mismatch between experiments is comparable to any mismatch between a given experiment and the simulation. In particular, a correlation analysis shows that the correlation coefficient between the saturations for both experiments ($\chi = 0.85$) is comparable to the correlation coefficient between experiments and simulations ($\chi = 0.78 - 0.82$). This again highlights the high sensitivity of these systems to initial and boundary conditions, which must be carefully considered when evaluating model success.

4.2. Viscous fingering ($\text{Ca} = 1.33\text{e-}4$)

In the previous subsection (Section 4.1), we showed that the numerical results are more consistent with experimental observations if the inlet length is extended. As such, the remainder of the simulations were carried out using an extended inlet length of $x_i = 300$ lu. Fig. 11 shows representative snapshots of CO_2 infiltration into the water-saturated micromodel at different times for $\text{Ca} = 1.33 \times 10^{-4}$, which is 5 times larger than the previous case. It can be seen, in Fig. 11 at $t^* = 0.37$, that for the experiments the invasion of CO_2 concentrates near the central portion of the porous section with very little invasion towards the edges, suggesting that the boundary effects are even more severe in this case owing to the higher flow rate. In the previous case ($\text{Ca} = 2.65 \times 10^{-5}$), when the CO_2 front arrived at the porous section its middle portion became pinned at the entrance of the porous section, simply because the pressure behind the CO_2 -water interface was insufficient to overcome the capillary resistance of the porous matrix. While the pressure was accumulating, the CO_2 front expanded in the lateral direction (stage I), leading to a flatter CO_2 front, which mitigated such boundary effects to some extent. On the other hand, in the current case, the bulk pressure gradient is higher; moreover, due to a higher Re , inertial effects are more significant, and the period for pressure accumulation is much shorter. Therefore, as soon as the middle portion of the CO_2 front arrives at the porous section, the invasion process begins almost immediately, even though the CO_2 front has still not extended laterally over the inlet of the porous section. This behavior is in contrast to the simulations, where some such effects are visible (*i.e.* the central fingers advance earlier and further than those close to the edges), but the effects are not as strong, again highlighting the clear importance of boundary conditions in this problem, which are next to impossible to replicate identically between experiment and simulation.

Aside from such boundary effects, the higher flow-rate case is fundamentally different than the previous case in two respects: first, it is evident that the fingering in this case is predominately

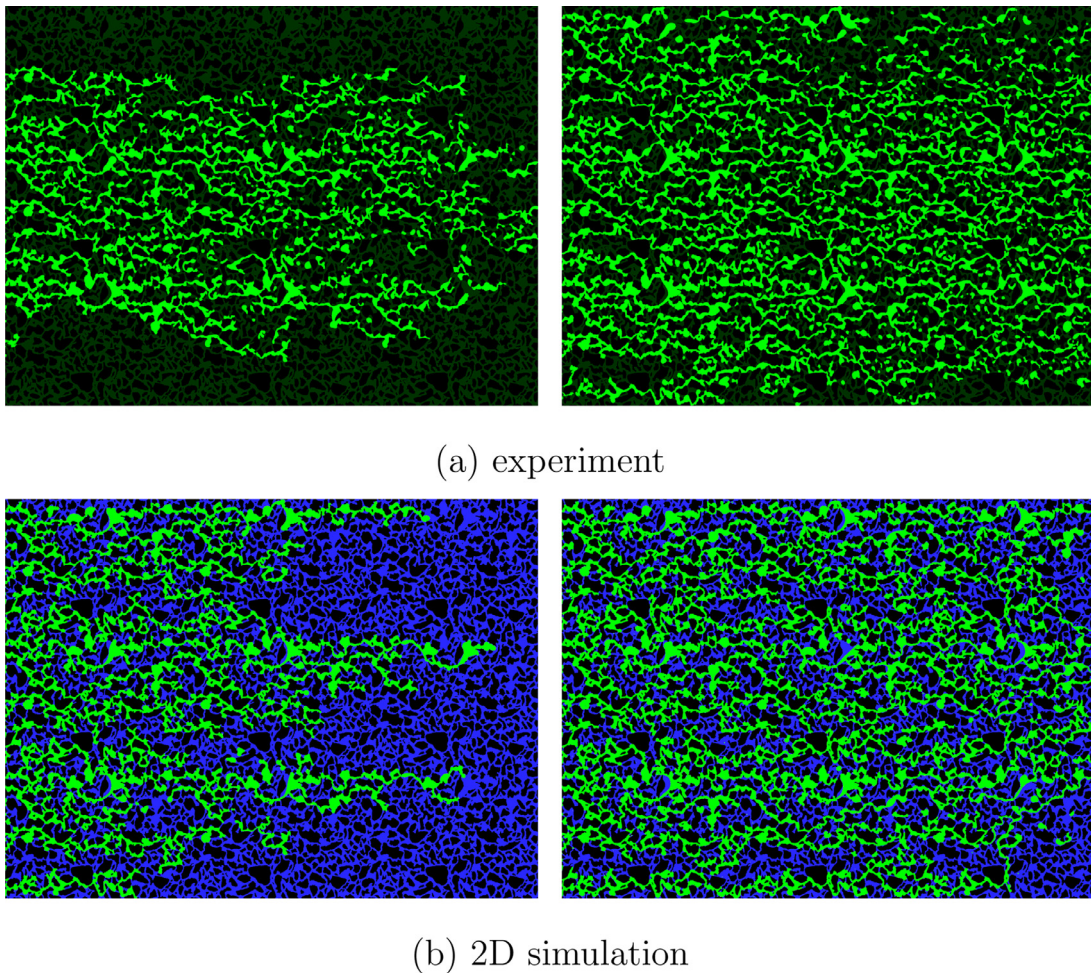


Fig. 11. CO₂ infiltration in the porous micromodel at $Ca = 1.33 \times 10^{-4}$. The column on the left shows the snapshot when CO₂ breaks through the end of the micromodel ($t^* = 0.37$), and the column on the right shows the quasi-saturated state ($t^* = 1.00$). Experiment (top row) versus simulation (bottom row). The experimental results show the depth-averaged concentration.

from left to right in line with the bulk pressure gradient with few fingers growing in other directions. This trend is indicative of viscous fingering only, which again is in agreement with the flow phase diagram of Zhang et al. (2011b). Second, the CO₂ saturation is higher in this case than that in the previous one, again, in agreement with previous studies (Cao et al., 2016; Zhang et al., 2011b). As the flow rate and the bulk pressure increase, inertial effects also increase, which facilitates the invasion of throats with higher capillary resistance (*i.e.* relatively smaller throats) (Moebius and Or, 2014); therefore, additional viscous fingers are formed, leading to a higher final CO₂ saturation as is evident in Fig. 12.

The temporal evolution of liquid CO₂ saturation in the entire porous section is shown in Fig. 12 for $Ca = 1.33 \times 10^{-4}$. A comparison is made between two experimental trials and simulation. As can be seen, the simulation agrees reasonably well with both sets of experimental data at early times when the CO₂ saturation is still growing. This is despite clear discrepancies that are shown for example in Fig. 11, where the experiment has no invasion along the edges of the micromodel. At later times, there is a deviation between the two experimental data sets as well as with the simulation result, attaining a lower final saturation than the experiments.

The spatial variation of liquid CO₂ saturation inside the porous micromodel at quasi-steady state ($t^* = 1.5$) is shown in Fig. 13 for $Ca = 1.33 \times 10^{-4}$. The general trend in the oscillatory behavior of the saturation profile is predicted in the simulations with comparable variability between peaks and troughs as well as horizontal

scales over which the variations occur when compared with experimental data. There are, however, some clear differences between simulations and experiment particularly near the inlet to the porous medium and at the outlet. This further highlights the clear influence of the boundary conditions, which at this higher flow rate seems to become even more important. Additionally there are visible discrepancies within the domain, in particular the valleys of simulation are lower than those of experiment data, in line with the previous observation of lower overall late time saturation (Fig. 12). Once more, a correlation analysis shows that the correlation coefficient between the saturations for both experiments ($\chi = 0.56$) is comparable to the correlation coefficient between the saturations predicted by the model and measured in the experiments ($\chi = 0.47 - 0.54$). The lower value of the correlation coefficient here compared to the previous case reflects a more challenging situation in terms of reproducibility, reflecting the highly sensitive nature of this flow under these unstable conditions.

5. Discussion on certain flow characteristics

One of the main benefits of working with high resolution numerical simulations is that one can resolve the velocity field throughout the flow domain. Previous experiments in both homogeneous (Kazemifar et al., 2016) and heterogeneous (Li et al., 2017) porous micromodels show that for multiphase flows asso-

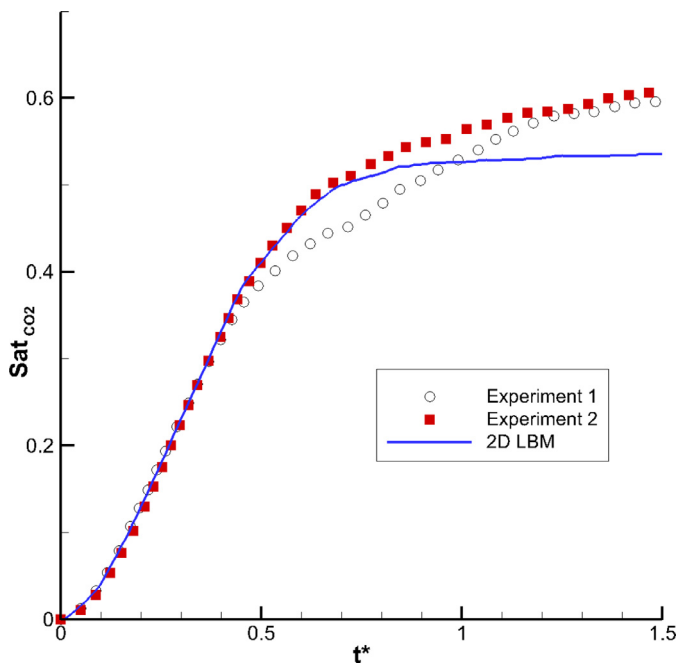


Fig. 12. Temporal variation of liquid CO₂ saturation: comparison between experiment and simulations for $Ca = 1.33 \times 10^{-4}$. Experimental data are shown by black circles and red squares, and the simulation result is shown with blue line. (For interpretation of the references to colour in this figure legend, the reader is referred to the web version of this article.)

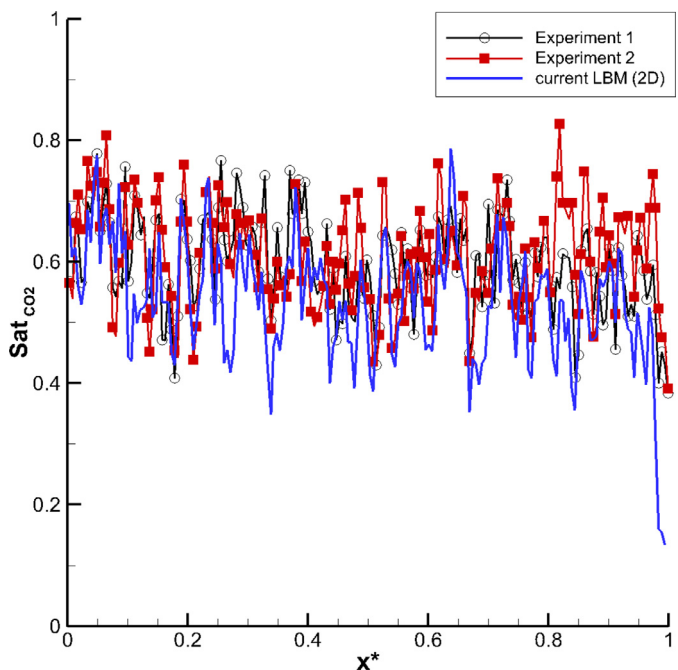


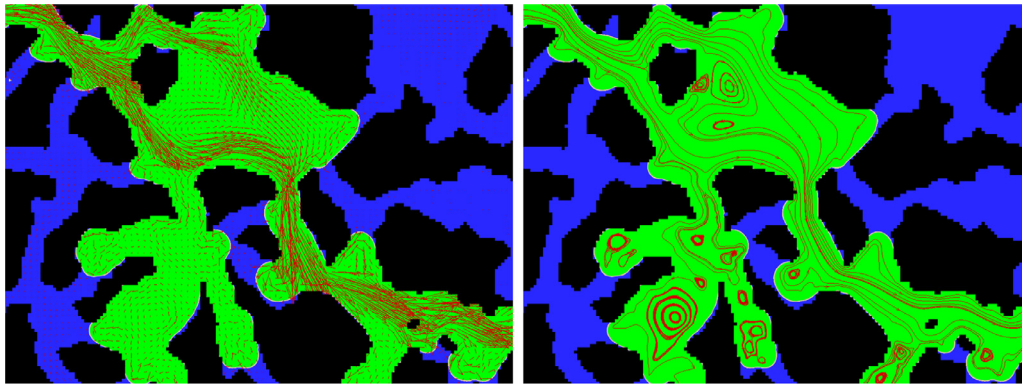
Fig. 13. The spatial variation of liquid CO₂ saturation inside the porous micromodel at quasi-steady state for $Ca = 1.33 \times 10^{-4}$. Comparison between the two experimental trials (black circles and red squares) and simulation (blue line). (For interpretation of the references to colour in this figure legend, the reader is referred to the web version of this article.)

ciated with conditions relevant to CO₂ sequestration, as studied here, inertial effects can become significant. The velocity field and streamlines in the flowing CO₂ phase in a select location within the porous section of the micromodel are shown in Fig. 14 at quasi-steady state for both $Ca = 2.65 \times 10^{-5}$ and $Ca = 1.33 \times 10^{-4}$. It is interesting to note that recirculation regions clearly exist at

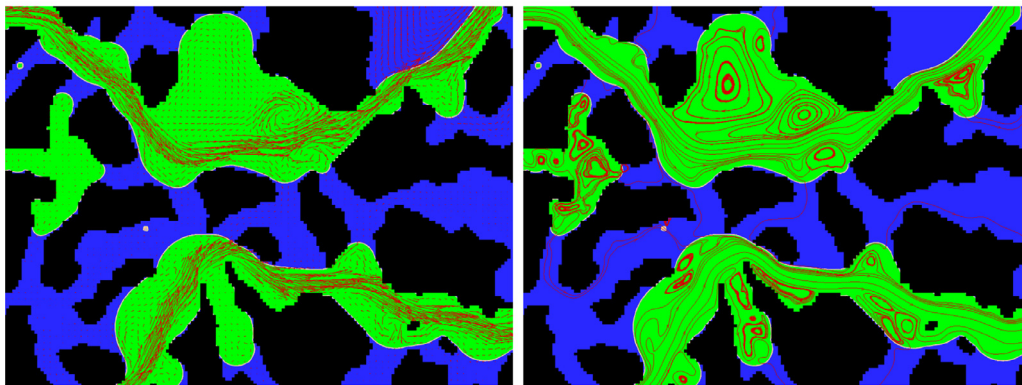
both flow conditions, although they appear to be larger and more significant in the higher flow rate case, perhaps due to stronger inertial forces. Note that the Reynolds number in the viscous fingering case ($Re_c = 3105$) is an order of magnitude larger than that in the capillary fingering case ($Re_c = 621$). It is important to recognize that, although the CO₂ and water phases have reached quasi-steady spatial configurations at this stage of the flow processes, the recirculation zones reported herein occur in the still-flowing CO₂ phase. While recent studies have reported the occurrence of recirculation zones within trapped fluid phases owing to high shear imparted at the fluid-fluid interface by the still-flowing phase (Kazemifar et al., 2016; Li et al., 2017), those identified herein are strong reflections of inertia, especially given their substantial sizes. This important observation is only possible when the detailed velocity field within the flowing phase CO₂ as shown in Fig. 14 can be accurately captured, which has rarely been reported before. Further, beyond simply being interesting to observe the emergence of recirculation in the still-flowing CO₂ phase, there are also practical consequences associated with this observation. Multiphase flows are known to strongly impact transport and mixing processes (e.g. Jiménez-Martínez et al., 2015; 2017; 2016) and the presence of recirculation zones is known to strongly influence the transport of dissolved substances in a porous medium (e.g., Bolster et al., 2009; 2014), which could have a strong impact when studying, for example, the longer term processes of dissolution of CO₂ into the water phase, which is considered an important permanent trapping mechanism of sequestered CO₂ (Gilfillan et al., 2009).

The identified recirculation zones clearly arise due to the manner in which the CO₂ phase distributes itself throughout the porous medium, creating “dead-end” like cavity and pore structures that are known to be conducive to creating such features. In order to believe that they emerge in the real flows and are not an artifact of the simulation, the local fluid phase distributions in simulations and experiments should display similar physical and structural characteristics. In particular, the distribution of the trapped residual water is key. Zhang et al. (2011b) highlighted four distinct forms in which the residual phase can be present: (i) Pools that occupy multiple pore bodies; (ii) thin films surrounding the grains; (iii) bridges between pore throats; and (iv) cones on the down-gradient side of silicon posts, which have also been observed in other experiments (Morais et al., 2016). Fig. 15 zooms in on a small section of the micromodel that displays many of these features. In particular, we focus on comparing the phase distributions at quasi steady-state between experiment and simulation. While some discrepancies clearly exist, most of the dominant features are well captured, and the distinct forms of trapped water exist in similar forms and sizes in both, including the water cone behind the large grain in the center of the image. Interestingly, it has been suggested that such cone structures are not thermodynamically stable and may merge with other structures during this “quasi-steady” phase (Zhang et al., 2011b).

Zhang et al. (2011b) suggested that the formation of such water cones is due to the high shear stress and drag force induced by the fast flow of the nonwetting phase, which in turn deforms a wetting film into the shape of a cone. On the other hand, Morais et al. (2016) attributed the formation of water cones to surface heterogeneities, which influence the behavior of the triple line. While both statements are reasonable explanations for water cones occurring at “quasi-steady” state, discussion on the dynamics associated with their formation is rare, presumably due to technical challenges in characterizing such flows (i.e. the very high spatial and temporal resolutions required in order to resolve this process). Here, our simulations and experiments provide a detailed view of the process as shown in Fig. 16. Interestingly, while the quasi-steady state in the simulations and experiments appear somewhat similar, the transient process of reaching this state dif-

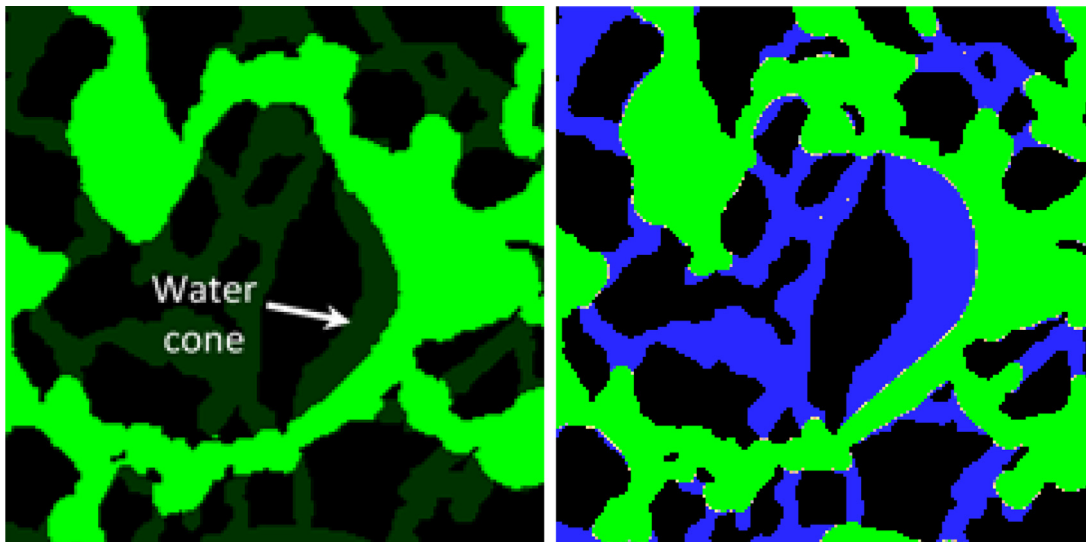


(a) capillary fingering



(b) viscous fingering

Fig. 14. Velocity vectors and streamlines at a select location within the porous micromodel. Comparison between capillary fingering at $Ca = 2.65 \times 10^{-5}$ and $Re_c = 621$ (top) and viscous fingering at $Ca = 1.33 \times 10^{-4}$ and $Re_c = 3105$ (bottom).



(a) experiment

(b) simulation

Fig. 15. Residual water within the micromodel after the drainage process at $Ca = 1.33 \times 10^{-4}$, illustrating the existence of water cones inside the porous micromodel for experiment (left) and simulation (right).

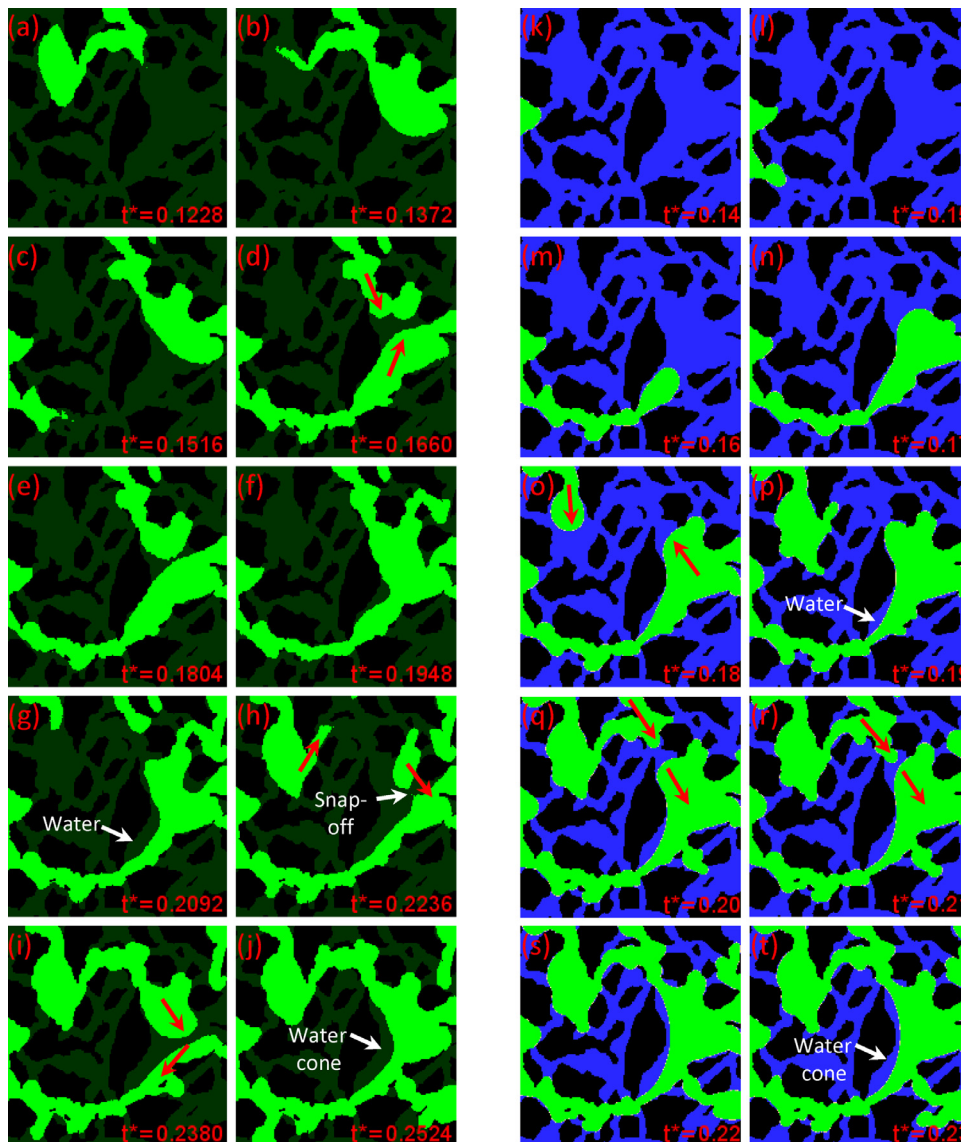


Fig. 16. Formation of a water cone for experiment (left) and simulation (right).

fers more, suggesting that the final saturation distribution is indeed controlled by pore-scale geometry and heterogeneities. Despite clear discrepancies in the detailed dynamics, both experiment and simulation suggest that the formation of a water cone is highly related to the interaction of two distinct CO_2 fingers. Of course, the porous matrix is highly hydrophilic and therefore the water tends to adhere to the solid surface.

As evident in Fig. 16 (d) and (o), two CO_2 fingers are attempting to enter the specific pore almost simultaneously, one through the top throat and the other one through the bottom throat. In the beginning, the bottom finger leads the process and enters around the grain (dimple-shaped) which displaces most of the water out of the pore, and leaves some behind in the dimple (g and p). However, as the top finger becomes stronger, the bottom one begins to recede (h, i, q, and r), driving more water back into the pore. When the top finger grows further, the two fingers eventually merge and a pocket of water is trapped within the pore, forming a water cone attached to the grain. Therefore, we conjecture the key elements that enhance the formation of water domes are strong surface hydrophilicity, high flow rate, and geometric

heterogeneity, suggesting that both Ref. Zhang et al. (2011b) and Ref. Morais et al. (2016) are correct.

It is worth reemphasizing that the final phase distribution around the pore is very similar between experiment and simulation, in spite of the clear discrepancies during the process of formation. For instance, the top finger grows much earlier in the experiment than that in the simulation, and a few snap-off events occurred in the experiment (g and h), but not in the simulation (note that our simulation is capable of capturing such snap-off events as evident in Fig. 11, just not in this case). We conjecture that such discrepancies are likely related to boundary effects as we mentioned multiple times before (*i.e.* the top finger is much closer to the centerline of the domain). We must note that it is merely a conjecture, but if correct this reinforces our idea that geometry has significant control over the final phase distribution, although the dynamics may take a rather different pathway. We have no way of formally proving this at this point in time, but hopefully future model-experiment comparisons will reveal whether this is correct or not.

6. Summary and conclusion

Using micromodel experiments and LBM simulations, we have studied multiphase flow through a heterogeneous porous medium at the pore scale under conditions relevant to geologic CO₂ sequestration. The pore geometry is based on a real sandstone, thus replicating more realistic pore structures than many previous micromodel studies. We have focused our study on two flow rates covering unstable flows in the range of crossover from capillary fingering to viscous fingering and viscous fingering regimes.

While there are clear discrepancies in the specific details of how the CO₂ distributes itself through the porous matrix both in space and time, there is reasonable agreement between the ultimate steady-state saturations predicted by the simulations and those measured in the experiments. In fact, a correlation analysis suggests that differences between model and experiment are comparable to differences between individual experimental trials. Given the unstable nature of the flow, such inter-experiment differences are to be expected, but the good agreement also highlights, unlike a flow through a homogeneous porous medium, that the instability and fingers that are formed are strongly controlled by the grain sizes and structure.

Additionally, differences between the experiment and simulation can also be attributed to differences in initial and boundary conditions. Due to inherent experimental uncertainties, it is nearly impossible to apply the exact same boundary conditions in our simulations, and given the sensitive nature of the flow, differences are to be expected. However, we also showed that better agreement was obtained when our simulations more faithfully represented the flow in the entrance region of the micromodel before the CO₂ even entered the porous region. Such a sensitivity to boundary and initial conditions suggests that efforts to improve detailed agreement between numerical simulations and experiments ad nauseam may be doomed to failure. We believe that instead efforts should be made to ensure that large-scale qualitative features are faithfully represented in such a way that may be useful for upscaling purposes or uncertainty quantification, although we acknowledge that it is not clear if this is genuinely possible without capturing all fine scale details. Of course, certain disagreements between the model and the experiments can also be attributed to limitations of the numerical model, which while promising, as with all models suffers numerical error and potentially incomplete physics (e.g. the diffuse interface approximation of the phase field model, while helpful for numerical stability may not be totally representative of the microscopic interface between phases; additionally it is well known that the density and viscosity of supercritical CO₂ are highly sensitive to pressure and temperature fluctuations, which is not accounted for in our model). Note for example that while some convergence testing was done, we did not conduct a comprehensive numerical convergence test as this was beyond our available computational resources. Additionally the numerical results presented in this manuscript are limited in that they are only 2D simulations, which cannot resolve inter boundary effects between the top and bottom plate. While we also developed 3D simulations, doing so comprehensively over the full time of the experiments (e.g., including the 300 lu entry length) was beyond our computational resources. However, our preliminary results suggest that certain improvements over the 2D results are achievable by resolving the third dimension (e.g., closer asymptotic saturations for our second experimental data set, since a 3D model is able to fill in patches of the porous medium that might be inaccessible a 2D model (Bhattad, 2010)).

A detailed view of the quasi-steady-state distribution of CO₂ and water shows a streamline structure that suggests a strong emergence of recirculating flows in the still-flowing CO₂ phase, which has multiple practical implications such as influencing the

transport of dissolved substances (e.g., potentially influencing dissolution dynamics). Additionally, it suggests that inertial effects are important, demonstrating potential limitations of upscaled multiphase flow models based on modified forms of Darcy's law, which neglects inertial effects. A further look also reveals that many important structural features are captured in both experiments and simulations, in particular relating to the diverse forms in which residual water can be trapped, including as a water cone, on the downstream side of grains. Using our temporally and spatially resolved data enables us to explore the formation of such water cones. Interestingly, while the final structure appears very similar in both experiments and simulations, the transient evolution differs. While we cannot prove it, we believe that this again suggests that geometrical features may be the key, rather than the fully detailed flow dynamics.

Thus, we have demonstrated that our proposed LB model is able to satisfactorily capture several important features of multiphase flow in a realistic pore geometry. In particular, our model is able to represent true physical properties, such as fluid density and viscosity, due to its ability to handle relatively large contrasts without having to un-physically alter the desired fluid properties. Additionally, while our experiments are able to study the evolution of the CO₂ through the micromodel with high temporal resolution, moving to study much higher flow rates, while maintaining such capabilities, will be challenging. By contrast, our numerical model has no such restriction and could be used to more effectively study larger flow-rate cases. Indeed, in the context of other complex flows (i.e. non-porous media) this model has been successfully used to simulate high Reynolds number flows (Fakhari et al., 2017a), which pose unique challenges under the conditions of large density and viscosity contrast (Fakhari and Bolster, 2017; Fakhari et al., 2017a).

Acknowledgments

The experimental portion of this work by Y.L. and K.C. was primarily supported as part of the Center for Geologic Storage of CO₂, an Energy Frontier Research Center funded by the U.S. Department of Energy, Office of Science, Basic Energy Sciences, under Award DE-SC0012504 (micromodel fabrication and half of the experiments and analysis). The modeling portion of this work by A.F. and D.B. was supported in part by NSF grant EAR-1351623. Work by Y.L., D.B. and K.C. (a portion of experiments, analysis and modeling) was also supported by the International Institute for Carbon Neutral Energy Research (WPI-I2CNER), sponsored by the World Premier International Research Center Initiative (WPI), MEXT, Japan. Y.L. also gratefully acknowledges partial support from the Center for Sustainable Energy at the University of Notre Dame (remainder of experiments and analysis).

Supplementary material

Supplementary material associated with this article can be found, in the online version, at [10.1016/j.advwatres.2018.02.005](https://doi.org/10.1016/j.advwatres.2018.02.005).

References

- Andrew, M., Bijeljic, B., Blunt, M.J., 2014. Pore-by-pore capillary pressure measurements using X-ray microtomography at reservoir conditions: curvature, snap-off, and remobilization of residual CO₂. *Water Resour. Res.* 50 (11), 8760–8774.
- Armstrong, R.T., Berg, S., 2013. Interfacial velocities and capillary pressure gradients during Haines jumps. *Phys. Rev. E* 88 (4), 043010.
- Ba, Y., Liu, H., Li, Q., Kang, Q., Sun, J., 2016. Multiple-relaxation-time color-gradient lattice Boltzmann model for simulating two-phase flows with high density ratio. *Phys. Rev. E* 94, 023310.
- Bachu, S., 2000. Sequestration of CO₂ in geological media: criteria and approach for site selection in response to climate change. *Energ. Convers. Manag.* 41 (9), 953–970.

- Bhattach, P., 2010. Transient study of the wetting films in porous media using 3D x-ray computed micro-tomography: effect of imbibition rate and pore geometry. PhD dissertation, Louisiana State University, Baton Rouge, LA.
- Blois, G., Barros, J.M., Christensen, K.T., 2015. A microscopic particle image velocimetry method for studying the dynamics of immiscible liquid–liquid interactions in a porous micromodel. *Microfluid. Nanofluid.* 18 (5–6), 1391–1406.
- Blunt, M., King, P., 1991. Relative permeabilities from two- and three-dimensional pore-scale network modelling. *Transp. Porous Med.* 6, 407–433.
- Bolster, D., Borgne, T.L., Dentz, M., 2009. Solute dispersion in channels with periodically varying apertures. *Phys. Fluids* 21, 056601.
- Bolster, D., Mēheust, Y., Borgne, T.L., Bouquain, J., Davy, P., 2014. Modeling preasymptotic transport in flows with significant inertial and trapping effects - the importance of velocity correlations and a spatial markov model. *Adv. Water Resour.* 70, 89–103.
- Cao, S.C., Dai, S., Jung, J., 2016. Supercritical CO₂ and brine displacement in geological carbon sequestration: micromodel and pore network simulation studies. *Int. J. Greenh. Gas Control* 44, 104–114.
- Chen, Y., Li, Y., Valocchi, A. J., Christensen, K. T., 2017. Lattice Boltzmann simulations of liquid CO₂ displacing water in a 2D heterogeneous micromodel at reservoir pressure conditions. In press. <http://dx.doi.org/10.1016/j.jconhyd.2017.09.005>.
- Chiu, P.-H., Lin, Y.-T., 2011. A conservative phase field method for solving incompressible two-phase flows. *J. Comput. Phys.* 230, 185–204.
- Chomsurin, C., Werth, C.J., 2003. Analysis of pore-scale nonaqueous phase liquid dissolution in etched silicon pore networks. *Water Resour. Res.* 39 (9).
- Connington, K., Lee, T., 2013. Lattice Boltzmann simulations of forced wetting transitions of drops on superhydrophobic surfaces. *J. Comput. Phys.* 250, 601–615.
- Connington, K.W., Lee, T., Morris, J.F., 2015. Interaction of fluid interfaces with immersed solid particles using the lattice Boltzmann method for liquid-gas particle systems. *J. Comput. Phys.* 283, 453–477.
- Ding, H., Spelt, P.D.M., 2007. Wetting condition in diffuse interface simulations of contact line motion. *Phys. Rev. E* 75, 046708.
- Fakhari, A., Bolster, D., 2017. Diffuse interface modeling of three-phase contact line dynamics on curved boundaries: a lattice Boltzmann model for large density and viscosity ratios. *J. Comput. Phys.* 334, 620–638.
- Fakhari, A., Bolster, D., Luo, L.-S., 2017. A weighted multiple-relaxation-time lattice Boltzmann method for multiphase flows and its application to partial coalescence cascades. *J. Comput. Phys.* 341, 22–43.
- Fakhari, A., Lee, T., 2013. Multiple-relaxation-time lattice Boltzmann method for immiscible fluids at high Reynolds numbers. *Phys. Rev. E* 87, 023304.
- Fakhari, A., Mitchell, T., Leonardi, C., Bolster, D., 2017. Improved locality of the phase-field lattice-Boltzmann model for immiscible fluids at high density ratios. *Phys. Rev. E* 96, 053301.
- Fakhari, A., Rahimian, M.H., 2010. Phase-field modeling by the method of lattice Boltzmann equations. *Phys. Rev. E* 81, 036707.
- Ferrari, A., Jimenez-Martinez, J., Borgne, T.L., Mēheust, Y., Lunati, I., 2015. Challenges in modeling unstable two-phase flow experiments in porous micromodels. *Water Resour. Res.* 51 (3), 1381–1400.
- Geier, M., Fakhari, A., Lee, T., 2015. Conservative phase-field lattice Boltzmann model for interface tracking equation. *Phys. Rev. E* 91, 063309.
- Gilfillan, S.M.V., Lollar, B.S., Holland, G., Blagburn, D., Stevens, S., Schoell, M., Cassidy, M., Ding, Z., Zhou, Z., Lacrampe-Couloume, G., Ballentine, C.J., 2009. Solubility trapping in formation water as dominant CO₂ sink in natural gas fields. *Nature* 458, 614–618.
- Gunstensen, A.K., Rothman, D.H., Zaleski, S., Zanetti, G., 1991. Lattice Boltzmann model of immiscible fluids. *Phys. Rev. A* 43, 4320.
- Gunter, W., Wiwehar, B., Perkins, E., 1997. Aquifer disposal of CO₂-rich greenhouse gases: extension of the time scale of experiment for CO₂-sequestering reactions by geochemical modelling. *Miner. Petrol.* 59 (1–2), 121–140.
- He, X., Luo, L.-S., 1997. Theory of the lattice Boltzmann method: from the Boltzmann equation to the lattice Boltzmann equation. *Phys. Rev. E* 56, 6811.
- Huang, H., Huang, J.-J., Lu, X.-Y., 2014. Study of immiscible displacements in porous media using a color-gradient-based multiphase lattice Boltzmann method. *Comput. Fluids* 93, 164–172.
- Huang, H., Sukop, M.C., Lu, X.-Y., 2015. *Multiphase Lattice Boltzmann Methods: Theory and Application*. Wiley-Blackwell.
- Huppert, H.E., Neufeld, J.A., 2014. The fluid mechanics of carbon dioxide sequestration. *Annu. Rev. Fluid Mech.* 46, 255–272.
- Jacqmin, D., 1999. Calculation of two-phase Navier-Stokes flows using phase-field modeling. *J. Comput. Phys.* 155, 96.
- Jacqmin, D., 2000. Contact-line dynamics of a diffuse fluid interface. *J. Fluid Mech.* 402, 57–88.
- Jiménez-Martínez, J., Anna, P.d., Tabuteau, H., Turuban, R., Borgne, T.L., Mēheust, Y., 2015. Pore-scale mechanisms for the enhancement of mixing in unsaturated porous media and implications for chemical reactions. *Geophys. Res. Lett.* 42 (13), 5316–5324.
- Jiménez-Martínez, J., Le Borgne, T., Tabuteau, H., Mēheust, Y., 2017. Impact of saturation on dispersion and mixing in porous media: photobleaching pulse injection experiments and shear-enhanced mixing model. *Water Resour. Res.* 53 (2), 1457–1472.
- Jiménez-Martínez, J., Porter, M.L., Hyman, J.D., Carey, J.W., Viswanathan, H.S., 2016. Mixing in a three-phase system: enhanced production of oil-wet reservoirs by CO₂ injection. *Geophys. Res. Lett.* 43 (1), 196–205.
- Karadimitriou, N., Hassanzadeh, S., Joekar-Niasar, V., Kleingeld, P., 2014. Micromodel study of two-phase flow under transient conditions: quantifying effects of specific interfacial area. *Water Resour. Res.* 50 (10), 8125–8140.
- Kazemifar, F., Blois, G., Kyritsis, D.C., Christensen, K.T., 2015. A methodology for velocity field measurement in multiphase high-pressure flow of CO₂ and water in micromodels. *Water Resour. Res.* 51 (4), 3017–3029.
- Kazemifar, F., Blois, G., Kyritsis, D.C., Christensen, K.T., 2016. Quantifying the flow dynamics of supercritical CO₂-water displacement in a 2D porous micromodel using fluorescent microscopy and microscopic PIV. *Adv. Water Res.* 95, 352–368.
- Koide, H., Tazaki, Y., Noguchi, Y., Nakayama, S., Iijima, M., Ito, K., Shindo, Y., 1992. Subterranean containment and long-term storage of carbon dioxide in unused aquifers and in depleted natural gas reservoirs. *Energ. Convers. Manage.* 33 (5), 619–626.
- Lallemand, P., Luo, L.-S., 2000. Theory of the lattice Boltzmann method: dispersion, dissipation, isotropy, Galilean invariance, and stability. *Phys. Rev. E* 61, 6546.
- Leclaire, S., Pellerin, N., Reggio, M., Trépanier, J., 2015. An approach to control the spurious currents in a multiphase lattice Boltzmann method and to improve the implementation of initial condition. *Int. J. Numer. Methods Fluids* 77, 732–746.
- Lenormand, R., Touboul, E., Zarcone, S., 1988. Numerical models and experiments on immiscible displacements in porous media. *J. Fluid Mech.* 189, 165–187.
- Lenormand, R., Zarcone, C., Sarr, A., 1983. Mechanisms of the displacement of one fluid by another in a network of capillary ducts. *J. Fluid Mech.* 135 (34), 337–353.
- Li, Y., Kazemifar, F., Blois, G., Christensen, K.T., 2017. Micro-PIV measurements of multiphase flow of water and liquid CO₂ in 2-D heterogeneous porous micromodels. *Water Resour. Res.*
- Linström, P.J., G, M.W., 2001. The NIST chemistry webbook: a chemical data resource on the internet. *J. Chem. Eng. Data* 46 (5).
- Liu, H., Valocchi, A.J., Kang, Q., 2015. Lattice Boltzmann simulation of immiscible fluid displacement in porous media: homogeneous versus heterogeneous pore network. *Phys. Fluids* 27, 052103.
- Liu, H., Valocchi, A.J., Werth, C., Kang, Q., Oostrom, M., 2014. Pore-scale simulation of liquid CO₂ displacement of water using a two-phase lattice Boltzmann model. *Adv. Water Res.* 73, 144–158.
- Lou, Q., Guo, Z., Shi, B., 2013. Evaluation of outflow boundary conditions for two-phase lattice Boltzmann equation. *Phys. Rev. E* 87, 063301.
- Martys, N.S., Chen, H., 1996. Simulation of multicomponent fluids in complex three-dimensional geometries by the lattice Boltzmann method. *Phys. Rev. E* 53, 743.
- Moebius, F., Or, D., 2014. Inertial forces affect fluid front displacement dynamics in a pore-throat network model. *Phys. Rev. E* 90 (2), 023019.
- Morais, S., Liu, N., Diouf, A., Bernard, D., Lecoutre, C., Garrabos, Y., Marre, S., 2016. Monitoring CO₂ invasion processes at the pore scale using geological labs on chip. *Lab. Chip* 16 (18), 3493–3502.
- Pacala, S., Socolow, R., 2004. Stabilization wedges: solving the climate problem for the next 50 years with current technologies. *Science* 305 (5686), 968–972.
- Perrin, J.-C., Benson, S., 2010. An experimental study on the influence of sub-core scale heterogeneities on CO₂ distribution in reservoir rocks. *Transport Porous Med.* 82 (1), 93–109.
- Porter, M.L., Schaap, M.G., Wildenschild, D., 2009. Lattice-Boltzmann simulations of the capillary pressure saturation interfacial area relationship for porous media. *Adv. Water Res.* 32, 1632–1640.
- Roman, S., Soulaire, C., AlSaud, M.A., Kovscek, A., Tchelepi, H., 2016. Particle velocimetry analysis of immiscible two-phase flow in micromodels. *Adv. Water Res.* 95, 199–211.
- Shan, X., Chen, H., 1993. Lattice Boltzmann model for simulating flows with multiple phases and components. *Phys. Rev. E* 47, 1815.
- Tartakovsky, A.M., Meakin, P., 2006. Pore scale modeling of immiscible and miscible fluid flows using smoothed particle hydrodynamics. *Adv. Water Res.* 29, 1464–1478.
- Zhang, C., Oostrom, M., Grate, J.W., Wietsma, T.W., Warner, M.G., 2011. Liquid CO₂ displacement of water in a dual-permeability pore network micromodel. *Environ. Sci. Technol.* 45 (17), 7581–7588.
- Zhang, C., Oostrom, M., Wietsma, T.W., Grate, J.W., Warner, M.G., 2011. Influence of viscous and capillary forces on immiscible fluid displacement: pore-scale experimental study in a water-wet micromodel demonstrating viscous and capillary fingering. *Energy Fuels* 25, 3493–3505.
- Zou, Q., He, X., 1997. On pressure and velocity boundary conditions for the lattice Boltzmann BGK model. *Phys. Fluids* 9, 1591.
- Zuo, L., Zhang, C., Falta, R.W., Benson, S.M., 2013. Micromodel investigations of CO₂ exsolution from carbonated water in sedimentary rocks. *Adv. Water Res.* 53, 188–197.